AGU ADVANCING EARTH AND SPACE SCIENCES

Water Resources Research

RESEARCH ARTICLE
10.1029/2025WR040778

Root Water Uptake Resolved by Distributed Moisture Storage Changes Through Soil and Weathered Bedrock

Dana A. Lapides[1], David N. Dralle[2], W. Jesse Hahm[3], William E. Dietrich[4], and Daniella M. Rempe[5]

[1]USDA-ARS Southwest Watershed Research Center, Tucson, AZ, USA, [2]USDA Forest Service Pacific Southwest Research Station, Davis, CA, USA, [3]Simon Fraser University, Burnaby, BC, Canada, [4]University of California, Berkeley, CA, USA, [5]University of Texas, Austin, TX, USA

Key Points:

- New method spatially resolves evapotranspiration and drainage using climate forcing and depth-distributed storage changes
- Mixed evergreen forest extracts water deeper within weathered bedrock as dry season progresses
- Deep drainage may continue even at the peak of the dry season

Supporting Information:

Supporting Information may be found in the online version of this article.

Correspondence to:

D. A. Lapides,
dana.lapides@usda.gov

Citation:

Lapides, D. A., Dralle, D. N., Hahm, W. J., Dietrich, W. E., & Rempe, D. M. (2025). Root water uptake resolved by distributed moisture storage changes through soil and weathered bedrock. *Water Resources Research*, *61*, e2025WR040778. https://doi.org/10.1029/2025WR040778

Received 15 APR 2025
Accepted 12 SEP 2025

Abstract Understanding how plants access water is critical to biosphere-atmosphere interactions. However, it remains challenging to resolve root water uptake in space and time. Here, we introduce (a) a mass balance method that uses depth-distributed moisture changes in the vadose zone to spatially resolve patterns of evapotranspiration (ET) and (b) an application of this method to a unique data set of continuous moisture dynamics across a deeply weathered root zone in a seasonally dry forest in coastal California. These observations are made possible by a Vadose-zone Monitoring System on a steep hillslope ("Rivendell") in the Angelo Coast Range Reserve. The new mass balance method accurately distinguishes between numerically generated vertically distributed ET and drainage fluxes. Synthetic tests across nine climate types show that the new method is broadly applicable in arid and Mediterranean regions. By applying the new mass balance method to the Rivendell data set, we determined spatiotemporal water fluxes in the deep root-zone at daily temporal resolution. Layers of the subsurface wet up simultaneously in the wet season. In the wet season, plant moisture for root water uptake was derived primarily from the soil. As the dry summer progresses, water uptake spreads to successively deeper depths until it occurs nearly equivalently across all depths. Water uptake at all depths across years is essentially the same, except in soil where water use patterns follow wet season precipitation patterns. Our results demonstrate that dry season unsaturated zone dynamics mediate the timing and magnitude of recharge to groundwater, with potential implications for summer streamflow.

1. Introduction

Root water uptake (RWU) is one of the largest fluxes in the terrestrial hydrologic cycle (Jasechko et al., 2013) but is a largely hidden process, embedded in soil and weathered bedrock. The depth distribution and timing of plant water uptake play an essential role in chemical weathering processes (e.g., Dontsova et al., 2020), nutrient cycling (e.g., Esfahani & Sonnewald, 2024), and respiration/carbon cycling (e.g., Gentine et al., 2019), making the vertical profile of plant water uptake an essential behavior in vegetation and hydrological models. Water uptake dynamics reveal plants' abilities to adapt to climate change and hint at impacts on hidden subsurface processes, such as recharge and streamflow. These insights are key for understanding contaminant transport, water resources, and groundwater modeling. Compared to depth-integrated total root water uptake for transpiration and annual-scale recharge, however, direct observations of the spatiotemporal dynamics of root water uptake and drainage are comparatively rare (Bachofen et al., 2024).

Exploration of when and where plants draw water is conducted using five main strategies: inference from root distributions (Lobet et al., 2014), tracers (e.g., Rothfuss & Javaux, 2017; Sprenger et al., 2016), optimization approaches (e.g., Guswa, 2008; Schymanski et al., 2008), root sapflow observations (e.g., Bachofen et al., 2024; Scott et al., 2008), and mass balance methods (e.g., Guderle & Hildebrandt, 2015; Lai et al., 2023). Each of these strategies requires making different assumptions about the relationship between root distributions and water uptake (Lobet et al., 2014), representativeness of isotopic samples for time- and depth-varying water sources (e.g., Rothfuss & Javaux, 2017; Sprenger et al., 2016), optimality principles (e.g., Guswa, 2008; Kleidon & Heimann, 1998; Protopapas & Bras, 1987; Schymanski, 2007; Schymanski et al., 2008), or other necessary simplifying assumptions. Observations of deep root distributions and isotopic profiles below a depth of 1 m are rare, which limits our knowledge of vadose zones that can extend deep into weathered bedrock (e.g., Hahm et al., 2020, 2022; Maysonnave et al., 2022; Rempe & Dietrich, 2018; Rose et al., 2003; Ruiz et al., 2010; Schwinning, 2010). Although the gold standard for deep unsaturated zone moisture dynamics observations has

historically involved neutron probes or nuclear magnetic resonance (e.g., Flint et al., 2002; Rempe & Dietrich, 2018; Schmidt & Rempe, 2020; F. Zhang & Zhang, 2021), these techniques require manual use and therefore have limited temporal resolution. Recently, techniques have been developed (e.g., Dahan et al., 2009) to deploy logging water content sensors throughout deep vadose zones. Such systems are still rare but provide a unique potential to capture daily patterns of root water uptake and drainage.

Mass balance techniques can be used to convert such time series of water content observations into fluxes. A general mass balance for the root zone can be written as (Dingman, 2015; Hillel, 2003):

$$\Delta S = P - ET - d, \tag{1}$$

where S is water storage, P is infiltrating rainfall or snowmelt, ET is evapotranspiration (including evaporation and root water uptake, RWU), and d is drainage out of the root zone. Typically, S and P are known from measurements, leaving two unknowns in the equation: ET and d. When working with multiple subsurface layers, P is replaced by drainage from the layer above. To close the mass balance, it is necessary to constrain ET or d, typically by working with physically based models (e.g., Portmann et al., 2013; Simunek et al., 1998; Wada et al., 2014), mixing models with tracers (Berghuijs et al., 2022; Jasechko et al., 2014), or inverse modeling approaches (Chai et al., 2023; Hupet et al., 2003; Musters & Bouten, 1999, 2000; Vrugt et al., 2008), or incorporating simplifying assumptions about the system that allow some terms to drop from the equation (Kosugi & Katsuyama, 2007; Schelde et al., 2011; Wilson et al., 2001). Guderle and Hildebrandt (2015) compared a set of techniques in the literature using synthetic timeseries of water content based on a site in Germany. They compared a single layer water balance to a multi-layer water balance (both assuming no drainage except during rainfall), a subdaily fluctuations method in which differences in nighttime and daytime values are used to infer ET (Li et al., 2002), and an inverse modeling approach. They found that the use of subdaily fluctuations in storage was most effective at capturing patterns of root water uptake followed by inverse modeling. However, the comparison performed by Guderle and Hildebrandt (2015) was performed using synthetic data based on a single site in Germany and only using the simplest type of mass balance approach, leaving further unknowns about how a more sophisticated mass balance would perform, and how each of these methods performs in seasonally dry environments, which may experience distinct water use strategies as the subsurface becomes very dry.

Here, we present two contributions to the observation of unsaturated zone water dynamics through (a) development of a new mass balance-based methodology for using depth-distributed moisture timeseries, in conjunction with surface water delivery (rainfall) and demand (potential evaporation), to resolve root-water uptake and drainage at each depth; and (b) a unique data set of depth-distributed water content observations throughout a deep unsaturated zone. We validate the new mass balance-based methodology against 1-D simulations in HYDRUS and compare performance to existing mass balance-based methods to ensure that the outcomes are realistic. This process allows us to validate performance on depth-distributed fluxes, which are generally unknown in field studies, and explore which climates these methods are applicable in. We then use the new mass balance method to calculate depth-distributed timeseries of root-water uptake and drainage at our field site, Rivendell. Here, we test the hypotheses: (a) that root water uptake proceeds in a top-down fashion (i.e., occurs at progressively deeper locations in the profile throughout the course of the summer dry season) under the mixed coniferous-broadleaf evergreen forest in the Northern California Coast Ranges and (b) whether root water uptake models based on water content or root distribution are able to capture the seasonal dynamics of uptake distributions at Rivendell.

2. Methods

This study is composed of two parts: (a) a synthetic test to compare mass balance methods for calculating depth-distributed ET and drainage fluxes across nine climate types and the study site and (b) an application of the method to field data. Section 2.1 describes the mass balance methods, which include two existing methods covered in Sections 2.1.1 and 2.1.2, and a new method in Section 2.1.3. All three methods are then tested against synthetic data produced using 1-D HYDRUS simulations (Section 2.2), similar to the testing framework employed by Guderle and Hildebrandt (2015). The synthetic test allows for detailed evaluation of the applicability of the mass balance methods in an environment where all fluxes and properties are fully known. Once we identify the most appropriate mass balance approach for processing water content data and which climate types it is

applicable in, we then apply this method to field data from our study site, Rivendell (Section 2.3). This process results in a set of depth-distributed timeseries of ET and drainage. We then use the ET timeseries to explore observed water uptake patterns and how they compare with simplified water uptake models used in earth systems models (2.5).

2.1. Mass Balance Methods

The goal of this study is to develop a rigorous method for producing data-driven, depth-distributed timeseries of drainage and ET. By splitting a vertical root zone column into discrete layers (Figure 1a) and neglecting any lateral fluxes (lateral fluxes are generally minimal in the vadose zone; Nimmo, 2006), we can write a mass balance for each layer as:

$$\Delta S_j = d_{j-1} - ET_j - d_j, \tag{2}$$

where ΔS_j is the change in storage at layer j, d_{j-1} is the flux into the storage layer—either as precipitation if it is the top layer or otherwise drainage from the layer above, ET_j is ET from the layer, and d_j is the drainage flux leaving the layer. Generally, it is possible to measure ΔS_j, precipitation in, and it is possible to estimate total ET over the whole column when flux towers are present and drainage to groundwater at annual scales, but layer-specific ET_j and d_j are unknown, especially when conducting the mass balance on short timescales. This is an unconstrained problem that requires additional assumptions to be solved. Here, we compare two existing methods (Method 1 (dry periods only) and Method 2 (power law drainage)) with a new method for constraining this mass balance (Method 3, which we dub "minimum drainage"). In the following, we review the existing methods and present the new method. It would have been ideal to include the method developed by Li et al. (2002) study in this work. However, as described in the text, we do not have sub-daily data at our field site due to sensor reliability. Thus, we chose to only work with methods that function with daily resolution data.

2.1.1. Method 1: Dry Periods Only

Following Equation 2, if spatially resolved drainage fluxes and storage changes are known, it is possible to calculate ET from all layers at all times. In the "dry periods only" method, the time period of analysis is restricted to times without recent rain or snowmelt (commonly in the past 24 hr), and it is assumed that all drainage terms are negligible (following Breña Naranjo et al. (2011), extended to multi-layer mass balance by Guderle and Hildebrandt (2015)). Then, Equation 2 simplifies to:

$$\Delta S_j = -ET_j, \tag{3}$$

and it is therefore straightforward to calculate ET fluxes, as shown in Figure 1b. The downsides to this method are: (a) there are gaps in the timeseries when rainfall or snowmelt occur, (b) there can be non-physical fluxes if storage increases during dry periods result in negative ET, and (c) there is no way to calculate drainage fluxes during wet periods since the method only functions in periods when drainage is assumed to be negligible. This method has been applied in a number of circumstances with some variation. For example, George et al. (2018) tested a variation in which they attributed all storage losses within 2 days of rainfall to drainage, but the ET calculations were nearly the same over the study period, so we use the simplest version of this method.

2.1.2. Method 2: Power Law Drainage

Rather than assuming negligible drainage during dry periods, drainage can be prescribed as a power law function of relative water content:

$$d_j = k_{sat}(t)\theta_j(t)^a, \tag{4}$$

where k_{sat} is the saturated hydraulic conductivity (known in HYDRUS simulations), $theta_j$ is the relative water content from 0 to 1 (when fully saturated), t is time, and a is a calibrated exponent, following Brocca et al. (2013) and Famiglietti and Wood (1994). This method is illustrated in Figure 1c. To apply this method, we calibrate a for

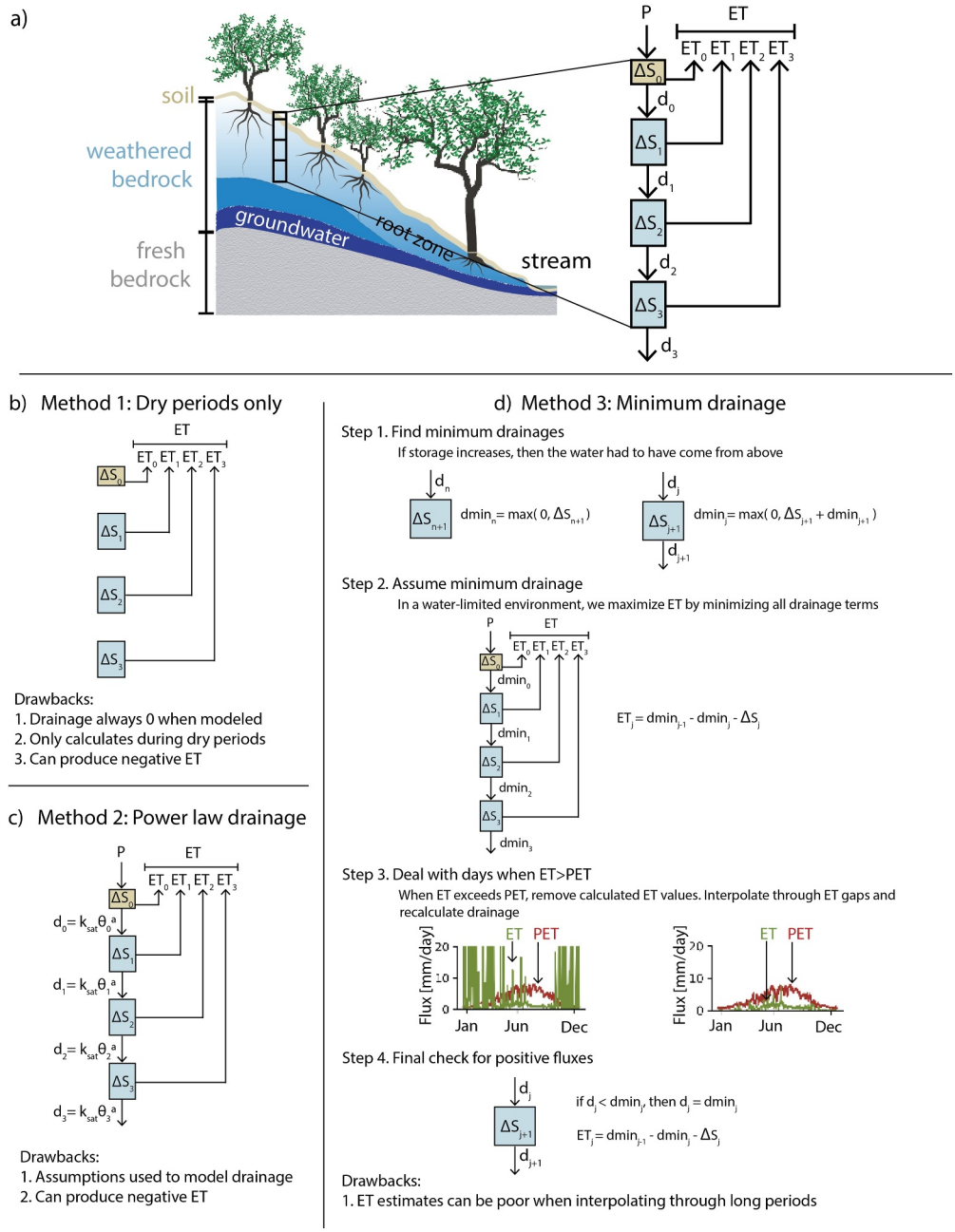

Figure 1. (a) Schematic diagram showing a typical vertical hillslope cross-section with a zoomed-in vertical column through the root zone. The vertical column is separated into four layers represented schematically by the boxes on the right. The number of boxes shown here is for explanatory purposes and does not represent the data used in this study. The darker blue region at the bottom of the weathered bedrock vadose zone indicates that the area is at field capacity. Precipitation (P) enters at the top of the column, and ET (ET_j, including evaporation and RWU) and drainage (d_j) leave from each layer (j). At every timestep, each layer has a change in storage (ΔS_j) such that the mass balance for the uppermost layer is $\Delta S_0 = P - d_0 - ET_0$, and for deeper layers $\Delta S_j = d_{j-1} - d_j - ET_j$. The sum over all ET_j is the total ET from the column. Panels (b)–(d) show schematic representations of each of the three mass balance techniques for estimating depth-distributed ET in a three layer system. In (b), precipitation and drainage are neglected, and the mass balance is calculated only in periods with no rainfall for at least 24 hr prior. In panel (c), drainage is calculated using a power law function of relative water content for each layer (θ_j). In panel (d), a minimum drainage is identified from each layer to account for positive storage changes below, following the four steps described in Algorithm 1 and Section 2.1.3.

the best performance on total ET (known in simulations), which is the most readily applicable approach possible with typically available field data. This calibration approach is similar to that used by Lai et al. (2023). Once a is calibrated, each ET_j is calculated using Equation 2. The downsides to this method are: (a) there can be nonphysical fluxes when calculated drainages into and out of a layer result in a negative ET_j, and (b) the drainage flux is calibrated to total ET over the study period, but daily rates are modeled with a functional form that is not directly data-driven and does not allow for layer-specific differences in drainage.

2.1.3. Method 3: Minimum Drainage Constraint

Method 1 constrains the mass balance by neglecting drainage terms. Method 2 models drainage terms using a power law. Method 3 uses water content observations to place a minimum bound on drainage terms. This method first takes advantage of the water content observations to place a minimum bound on all of the drainage terms based on the following principle: if storage increases somewhere in the profile, then that water must come from above. Then, we assert that all drainage terms are equal to the minimum drainages and calculate all ET terms from mass balance. Finally, we correct any non-physical fluxes to produce a final set of depth-distributed ET and drainage fluxes that maximize ET from the system given the observations and physical limitations. We describe Method 3 algorithmically in Algorithm 1 and in text as follows. For a detailed example of how this method works, see Supporting Information S1.

Step 1: *Find minimum drainage.*

We track storage changes across layers 0 to n + 1, treating n + 1 as a boundary condition. We therefore use n to refer to the deepest layer included in the full mass balance calculation. If the bottom boundary condition box (box $n + 1$) gains water, then this water must have come from above. Using this logic, we can find a minimum bound for the drainage flux entering box $n + 1$ at each timestep as:

$$dmin_n = \max(0, \Delta S_{n+1}), \tag{5}$$

where $dmin_n$ is the drainage flux leaving box n. Since we are unable to constrain drainage leaving from box $n + 1$, we do not compute timeseries at that layer. We only use the deepest water content measurements to constrain drainage from the layer above.

At this point, we have a timeseries of $dmin_n$. Now, let's look at box n, directly above the boundary condition box $n + 1$. If storage increases in box n, then, similarly, this water had to have come from above. Further, drainage entering from above must also be sufficient to account for the minimum drainage leaving box n. In general, this means for box $0 \leq j \leq n$:

$$dmin_j = \max(0, \Delta S_{j+1} + dmin_{j+1}). \tag{6}$$

We continue this process moving upwards until we reach the top of the column. Flux $dmin_{-1}$ entering the top box corresponds to rainfall. Rainfall is a reliable observation; however, it typically needs to be processed to remove interception losses and account for undercatch. As a result, using observed precipitation data for net precipitation (infiltration) timeseries may not be perfectly accurate. When observed precipitation is insufficient to meet $dmin_{-1}$, precipitation is increased. This change is required to close mass balance if we assume that water content observations are accurate and that there are no lateral or upward fluxes. At our study site, these precipitation increases account for 7% of annual precipitation, which is comparable to uncertainty of tipping bucket rain gauges in steep terrain (Cauteruccio et al., 2021). A precipitation decrease is never required since there is never too much precipitation for mass balance. Excess precipitation would just pass through the profile as drainage. We now have, for each box 0 through n, the change in storage at each timestep (observed) and minimum fluxes entering and leaving the box (inferred as just described).

Algorithm 1: Algorithmic description of Method 3 (Minimum drainage constraint method) for processing water content data into depth-distributed *ET* and *d* timeseries. *n* is the number of subsurface layers used for analysis, $dmin_j$ the minimum drainage from layer *j* required to allow all fluxes to be positive, ΔS_j the storage change at layer *j*, d_j the drainage from layer *j*, ET_j the *ET* from layer *j*, *PET* the total column potential *ET*, $ET_{j,interpolated}$ an interpolated *ET* timeseries for layer *j*, *seven_day_median*() a function that uses a moving window approach to get the 7-day median value for each timestep, and *linear_interpolation*() a function that fills NULL values with a linear interpolation. By convention d_{-1} is the precipitation flux entering the column.

Step 1: Find minimum drainage
$dmin_n$ = max(0, ΔS_{n+1})
for j = n to 0 **do**
    $dmin_{j-1} \leftarrow \max(0, \Delta S_j + dmin_j)$
end for

Step 2: Assume minimum drainage
for each layer j **do**
    $d_j \leftarrow dmin_j$
    $ET_j \leftarrow d_{j-1} - d_j - \Delta S_j$
end for

Step 3: Deal with days when $ET > PET$
for each timestep t **do**
    if $\Sigma_j ET_j(t) > PET(t)$ **then**
        for each layer j **do**
            $ET_j(t) \leftarrow$ NULL
            $d_j(t) \leftarrow$ NULL
        end for
    end if
end for
for each layer j **do**
    $ET_{j,interpolated} \leftarrow linear\_interpolation(seven\_day\_median(ET_j))$
end for
for each timestep t **do**
    for each layer j **do**
        if $ET_j(t) ==$ NULL **then**
            $ET_j(t) \leftarrow ET_{j,interpolated}(t)$
            $d_j(t) \leftarrow d_{j-1}(t) - ET_j(t) - \Delta S_j(t)$
        end if
    end for
end for

Step 4: Final check for positive fluxes
for each timestep t **do**
    for each layer j **do**
        if $d_j(t) < 0$ **then**
            $d_j(t) \leftarrow dmin_j(t)$
            $ET_j(t) \leftarrow d_{j-1}(t) - d_j(t) - \Delta S_j(t)$
        end if
    end for
end for

Step 2: *Assume minimum drainage*.

Next, we consider a seasonally dry, Mediterranean climate. Since the system is water-limited during the dry summer growing season, then we expect the maximum ET allowed by the observations to be a good estimate for

ET. We find the maximal ET by assuming that all drainage terms are equal to the minimum drainage from Step 1. Then, we calculate each depth-distributed ET_j from mass balance as:

$$ET_j = mind_{j-1} - mind_j - \Delta S_j. \quad (7)$$

ET from the profile is maximized so long as drainage leaving at the bottom of the profile is minimized. Then, all other storage decreases are attributed to *ET*. During dry periods when *ET* is most important, drainages tend to be small, so redistribution of water within a daily timestep should be small relative to ET, meaning that Equation 7 can be understood as a good estimate for maximum *ET* from each layer.

Step 3: *Deal with days when ET > PET*.

The assumption in Step 2 is based on considering a water-limited environment; however, not all days are water-limited. When it is raining or has recently rained, there is more than enough water available to meet demand. On these days, the maximal ET allowed by observations is not a good estimate for the actual ET. So, on days when ET_{total} exceeds *PET* (calculated using the Hargreaves method; Hargreaves & Samani, 1985), we replace all ET_j and d_j with null values. Typically, ET_{total} for a day is either less than *PET* or at least a factor of 2 greater, so the method of determining *PET* has little impact on results. We then fill the gaps in each ET_j timeseries using a linear interpolation between 7-day median ET_j values. Finally, null values in d_j timeseries are filled in using Equation 2. This is the only way using Method 3 that d_j can exceed $dmin_j$. *PET* alone is insufficient to estimate ET_j during these gaps since *PET* provides only a total column value and not a layer-specific estimate. As a result, a gap-filling method is necessary in order to partition reasonable water use across depths, and a linear interpolation is a parsimonious approach. Due to the use of interpolation, this method is best applied in areas where either (a) most ET occurs during dry periods so that errors in wet periods are small relative to total annual ET or (b) wet periods are short so that interpolated periods are short.

Step 4: *Final check for positive fluxes*.

After Step 3, there are days when layer-specific drainages are smaller than the minimum drainages calculated in Step 1, resulting in forced negative fluxes of ET_j or d_j throughout the column. Where $d_j < dmin_j$, we replace the daily value of d_j with $dmin_j$ and recalculate ET_j fluxes from mass balance accordingly. This step does not result in excessively high ET_{total} since we strictly increase drainage at this step, resulting in strictly less ET_{total}.

2.1.3.1. Limitations and Assumptions.

In Method 3, we explicitly consider a seasonally dry, Mediterranean climate. Since the system is water-limited during the dry summer growing season, Method 3 produces the greatest total *ET*, consistent with observational data and *PET* limitations. The following additional assumptions are used:

1. Lateral flows are negligible
2. All ET_j are non-negative
3. Water does not flow upward in the profile (all d_j are non-negative), meaning no vertically upward capillary rise, groundwater intrusion, or hydraulic redistribution can occur.

Lateral flows are generally minimal in the unsaturated zone (Nimmo, 2006); this method is not applicable in profiles with significant lateral flows. *ET* terms are positive by definition. Upward water fluxes (e.g., root-mediated hydraulic redistribution) may be important in some contexts. Root-mediated hydraulic redistribution should be most important during dry periods, when water would move from wet, deep layers to dry, shallow layers. This is the period when *ET* is greatest in a Mediterranean environment. Hydraulic redistribution may move 0.25–0.5 mm/d (G. Yang et al., 2022), which could result in 10%–20% error in *ET* at our study site. This method may not be appropriate at sites where hydraulic redistribution accounts for a large portion of daily water use. Assumptions 1 and 3 are also implicit to Methods 1 and 2, meaning that these limitations are common among mass balance methods.

The downsides to this method are: (a) mass balance errors can occur if precipitation needs to be increased to account for storage changes below, but this would result in a mass balance error in any method neglecting upward and lateral fluxes, and (b) ET_j and d_j estimates become poorer in very wet times when there are long periods of interpolation between dry days. The latter makes the method particularly well-suited to application in areas with Mediterranean climates or desert climates with short rainy periods so that there is little precipitation delivery

during the growing season. Performance may be significantly reduced for other climate types, as is explored in the synthetic evaluation. Method 3 (minimum drainage) is the only method of the three presented here that is capable of producing both d_j and ET_j timeseries for all times with no process assumptions (Guderle & Hildebrandt, 2015) tested additional methods; however, all additional proposed methods required either subdaily data or more complicated models with process assumptions. Since our goal is to learn about process from the data, we are testing methods that do not require detailed process assumptions.

2.2. Synthetic Evaluation

There are no existing field measurements of depth-distributed timeseries of d_j and ET_j to test the methods described in Section 2.1. Guderle and Hildebrandt (2015) used a synthetic model framework to test a set of methods with a climate representative of a site in Germany. Here, we test a subset of those methods that do not require sub-daily data or process assumptions (Methods 1 and 2) along with a new method (Method 3: minimum drainage constraint) against synthetic data based on locations across the nine main climate types present in the Conterminous United States and a field site in Northern California (Figure 5a). Below, we describe the synthetic model used for testing (Section 2.2.1) and the evaluation framework (Section 2.2.2).

2.2.1. Model Description

We evaluate each of the three methods against 2-year timeseries of ΔS_j, ET_j, and d_j calculated using HYDRUS-1D (Simunek et al., 1998) via the python API Pyhydrus (https://github.com/phydrus/phydrus) at each of the nine representative climate locations and the study site (Rivendell). Parameters and boundary conditions are described in Table S2 in Supporting Information S1. We prescribed root water uptake potential to be constant across the first meter of depth and then to linearly decrease to a depth of 6 m, below which root water uptake potential is 0. The root water uptake potential describes the relative ability for roots to draw water from different depths, so this functional form allows for the greatest water uptake at shallow depths with decreases to a depth of 6 m and no root water uptake below 6 m. This model does not accurately represent the water uptake profile at a specific site but is designed to capture water use patterns that span a deep unsaturated zone. This exercise is meant as a test for how well the mass balance models can recover depth-distributed ET and drainage timeseries rather than an attempt at using HYDRUS to reproduce our site data or any particular site data. Potential root water uptake from each depth varies over time as a function of potential evapotranspiration. The root uptake model applied was that of Feddes et al. (1978). Details on root water uptake in HYDRUS are described by Simunek et al. (1998). Generally, root water uptake is given by:

$$S(h) = \alpha(h) S_p, \tag{8}$$

where S [cm] is the root water uptake from a given depth, h the soil water pressure head [cm], S_p [cm] the potential transpiration from a given depth, and α a dimensionless function (from 0 to 1) that indicates the fraction of potential transpiration actually taken up by plants.

We use 10 sets of precipitation and potential transpiration timeseries from the sites marked in Figure 5a. Nine sets are chosen to represent the nine different major climate types from the Koppen-Geiger climate classification (Köppen & Geiger, 1928) found across the Conterminous United States. See Table S3 in Supporting Information S1 for site characteristics. For these sites, a point was chosen from within the area covered by each climate type, and precipitation and potential evapotranspiration timeseries were obtained from gridMET (Abatzoglou, 2013) for a 100 km buffered region around each point using Google Earth Engine (Gorelick et al., 2017). The study site (Rivendell at the Eel River CZO, see Section 2.3.1 for more details) is found within the Mediterranean climate region, but we also perform a 10th test of the mass balance methods against HYDRUS using the precipitation timeseries for Rivendell. For all synthetic tests, we used the precipitation timeseries for years 2017 and 2018, with 15% of precipitation removed to represent interception (Salve et al., 2012). The potential transpiration for the Rivendell test is calculated using the Hargreaves method (Hargreaves & Samani, 1985), as calculated in La Follette et al. (2022). For simplicity, in all cases, potential evapotranspiration is all attributed to potential transpiration, and potential soil evaporation is neglected. All outputs are recorded at 25 cm vertical depth intervals. Moisture timeseries at select depths for the HYDRUS simulation based on the study site (Rivendell) are shown in Figure S7 in Supporting Information S1.

2.2.2. Synthetic Evaluation

From HYDRUS, we have full information about all inputs, all subsurface properties, and all fluxes in the system. To test each of the mass balance methods, HYDRUS nodes were consolidated into three sets of layers with resolutions of 25, 50, and 100 cm to test the impact of layer thickness (vertical data resolution) on results. We also performed each mass balance method with all possible numbers of layers starting with just the shallowest layer and adding layers until the full column was used for calculation. This set of calculations allowed us to evaluate how vertical resolution and maximum depth impacted results. Each mass balance method is a routine without tunable parameters (excepting the exponent in the power law drainage for Method 2). The only way to alter results from the routines is to adjust the maximum depth used for calculation and the resolution of data, so we test the impact of these two methodological choices. Performance of each method was measured using four metrics: (a) mean absolute error (MAE) and (b) Kling-Gupta Efficiency (KGE; Gupta et al., 2009) between ET_j and d_j timeseries for each layer and for total ET summed over the column; (c) fraction of timeseries with missing output data; and (d) mass balance error. For Methods 1 and 2, mass balance error was calculated as the sum of all negative ET_j terms over the timeseries. For Method 3 (minimum drainage), mass balance error is the sum of all precipitation increases applied to meet storage increase requirements from below. However, because HYDRUS-1D perfectly conserves mass, has no measurement error, and includes no lateral fluxes, mass balance error for Method 3 (minimum drainage) is always 0. For all methods, sensitivity to vertical data resolution was negligible (see Text S5 in Supporting Information S1), so all results are shown with the highest vertical resolution (25 cm) in the main text. There is a very small loss in performance with coarsening resolution. Higher sensor density can provide greater information, allowing for greater accuracy, which may be necessary in sites that are highly variable with depth. In a more homogenous situation, such as in the HYDRUS simulations, resolution is less important. Summary results are shown for the nine climate types, and detailed results are shown for the Rivendell site.

2.3. Applying the Minimum Drainage Constraint Mass Balance Method to Observational Data

The synthetic evaluation described in Section 2.2 is used to identify the appropriateness of mass balance methods for application to real data. With confidence in the method for a climate representative of our study site, we proceed to apply it to field data.

2.3.1. Site Description

The instrumented hillslope (Rivendell) drains to Elder Creek, a 16.9 km^2 intensively studied watershed underlain by mudstones and sandstones of the Coastal Belt of the Franciscan Formation in the Northern California Coast Range (Figure S13a in Supporting Information S1). The site receives around 2,000 mm of annual precipitation, mostly as rain between November and April that is offset from the peak growing season in June–August (Figure 2a). Rivendell is a steep hillslope (average 32°) mantled by a thin soil, which is underlain by a weathered bedrock zone that thins from 23 m at the divide to less than 4 m near the base of the hillslope (Rempe & Dietrich, 2014). Seasonal recharge of groundwater passes through this zone (Rempe & Dietrich, 2018; Salve et al., 2012). A seasonal water table develops at the fresh bedrock underlying the weathered bedrock and typically rises by many meters during the wet season, but in no instance does it reach the surface, even at low slope positions. Overland flow has not been observed at the site, and lateral flows are considered negligible within the deep unsaturated zone, since saturation is not observed above the water table and unsaturated flows are driven primarily by gravity and matric forces (Nimmo, 2006). This thick profile allows for ample water to support a dense evergreen forest (Hahm et al., 2019). Interception is approximately 10%–20%, and the remaining rainfall infiltrates, where it contributes to increasing soil and weathered bedrock water storage (Figure 2b) and recharges the hillslope groundwater aquifer (see rising water table in Figure 2c, Dralle et al., 2023). The seasonal groundwater flows laterally to channels to generate streamflow (Dralle et al., 2018). Each year, water content continues to increase at deeper depths after rainfall stops (see storage rise in Figure 2b continuing after the dotted line each year), suggesting that some drainage continues during the dry season. Peak storage (Figure 2b) roughly coincides annually with peak PET (green in Figure 2a) and drops rapidly until the start of the subsequent wet season (vertical dashed line).

Table S1 in Supporting Information S1 describes all data used and produced in this study. To track rock moisture content and sample rock moisture, the site hosts a Vadose-zone Monitoring System (VMS), which consists of a pair of flexible sleeves installed in parallel holes drilled at a 55° angle into the slope and subsequently held in

10.1029/2025WR040778

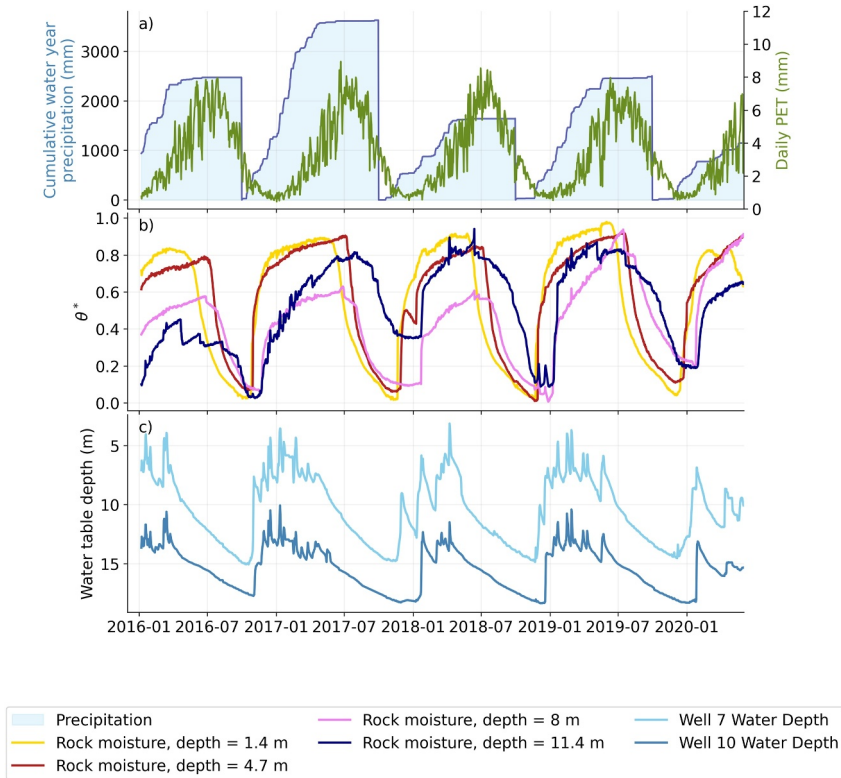

Figure 2. (a) Cumulative water year precipitation (blue) and daily potential evapotranspiration (green) at Rivendell. (b) Normalized relative water content (from 0 (min) to 1 (max), θ^*) at four representative depths in the VMS. Data are available at approximately 1.5 m intervals to a depth of 15 m. (c) Water table depth at nearby wells, with locations shown in Figure S13 in Supporting Information S1. Vertical dashed lines mark the start of the wet season each year, and dotted lines mark the end of significant rainfall for each water year.

place by filling with concrete. Locations of the Angelo Meadow Weather Station, soil moisture probes, wells, and the VMS sleeves are marked in Figure S12a in Supporting Information S1).

Flexible time domain transmission (TDT) sensors and flexible, custom lysimeters are distributed along the length of each sleeve of the VMS to measure water content and collect water samples (Figure S13b in Supporting Information S1). This design allows for data collection at about 1.5 m vertical resolution to a depth of 15 m that can be approximated as a single vertical column assuming no significant spatial heterogeneity at the 15 m lengthscale. 10 monitoring wells (Oshun et al., 2016) are distributed across the hillslope with approximately monthly neutron probe surveys (Rempe & Dietrich, 2018). Wells 7 and 10 are closest (downslope and upslope) to the VMS (Figure S12a in Supporting Information S1). Wells 7 and 10 were used to monitor groundwater levels. Well 10's water table ranges from 18 m (dry season) to 13 m (wet season), while Well 7 ranges from 15 to 7 m. The inferred water table at the VMS site ranges from 17 to 12 m depth, meaning only depths shallower than 12 m are unsaturated and used in our analysis.

121 individual TDR probes installed in vertical profiles and across the hillslope provided continuous data throughout the study period (Bilir et al., 2021; Oshun et al., 2016; Salve et al., 2012). In this study, we use data from 6 TDR near to the VMS (locations marked in Figure S12a in Supporting Information S1) with depths ranging from 27 to 33 cm. Locations and summary information about Wells 7 and 10 and the most complete and relevant TDR data are included in Text S5 in Supporting Information S1. Full maps and descriptions of instrumentation can be found in Rempe and Dietrich (2018), Oshun et al. (2016), and Salve et al. (2012). To quantify the total water storage capacity at the VMS, we use neutron probe data (Rempe & Dietrich, 2018). Neutron counts collected at 25 cm depth intervals in each borehole at the site are used to calculate the change in water content at approximately monthly frequency (Well 7 and 10 marked in Figure S13a in Supporting Information S1). While data were taken at both Well 7 and Well 10, Well 10 data have not yet been processed into water contents, so we use neutron counts only from

Well 7. We use these data to validate the spatiotemporal patterns of moisture content provided by the TDT sensors. To capture the temporal dynamics of plant water use we use sapflow data collected across the Rivendell hillslope (Bilir et al., 2021). Both neutron probe and sapflow data are used as a comparison to calculated patterns of ET (including evaporation and RWU) using mass balance methods.

We use a PET timeseries calculated by La Follette et al. (2022) using the Hargreaves method (Hargreaves & Samani, 1985). The study period extends from January 2016–December 2019, which was an unusually wet period at Rivendell with an annual precipitation of 2,500 mm.

2.3.2. Calculating Depth-Distributed ET and Drainage Fluxes

We applied Method 3 (minimum drainage constraint) to analyze field data from Rivendell, calculating depth-distributed ET_j and d_j timeseries. The analysis used precipitation data from the Angelo Meadow Weather Station and TDR and TDT storage timeseries from soil and VMS port depths at approximately 1.5 m vertical resolution. Precipitation measurements were reduced by 15% to account for interception losses and adjusted for undercatch using the D. Yang et al. (1998) formula.

Raw TDT and TDR measurements exhibited drift throughout the study period and significant noise at the subdaily scale. Rather than a diurnal pattern of water content, the subdaily values look like random noise. To address the subdaily sensor noise, we converted all water content data to daily values by taking the mean. The uncertainty in these daily averages was minimal, staying below 0.01 in water content (typically less than 1% of the daily value). We then subtracted a linear curve fitted to the set of annual minimum water contents. This correction preserved natural variations in annual minimum and maximum values while eliminating the systematic drift.

The drift-corrected curves were then normalized from 0 to 1:

$$\theta_j^* = \frac{\theta_j - \theta_{j,\min}}{\theta_{j,\max} - \theta_{j,\min}}, \tag{9}$$

where θ_j^* is the normalized water content at layer j, θ_j is the daily, drift-corrected water content data, $\theta_{j,\min}$ is the minimum θ_j throughout the study period, and $\theta_{j,\max}$ is the maximum θ_j throughout the study period. Sample θ_j^* curves are shown in Figure 2b. Since the shallowest VMS depth is 1.95 m, we took the mean θ^* value across all nearby soil moisture probes (Level 3 TDR) in representative material to represent subsurface storage in the soil. There are differences in soil moisture response among the probes. For soil moisture timeseries and how the differences among timeseries impact study results, see Text S7 in Supporting Information S1. At this point, we have a normalized water content timeseries for each depth from 0 to 1. Some depths have much larger dynamic storage than others, though, so we need to scale each depth to an appropriate absolute amount of variability.

To do so, we converted normalized water content values to actual water storage by multiplying them by layer-specific storage capacities, where soil storage capacity (80 mm) was estimated based on local measurements, and rock moisture storage capacity (425 mm total) was distributed exponentially with depth based on neutron probe data from Well 7 (the closest well with neutron probe surveys). The storage capacities were calibrated using previously published measurements of maximum dry season drawdown across multiple wells (Rempe & Dietrich, 2018), with the VMS location's higher storage capacity reflecting its deeper unsaturated zone compared to the reference Well 7 (closest well with processed water content, storage capacity 220 mm). The assignment of storage capacity has a large impact on the model outcomes, making it by far the most sensitive part of the process and the most likely place where bias could enter. We have done our best to assign storage capacities based on the best available data. Using the range of observed storage patterns across the hillslope reported in Rempe and Dietrich (2018), we found that patterns of uptake and drainage were similar. Annual drainage varied by less than 10%, and annual ET varied by less than 20%. In the main text, we show findings only for the storage capacity that best matches observations. More details and an exploration of how different storage capacity assignments impact results can be found in Text S5 in Supporting Information S1.

Once all the storage timeseries were prepared, we calculated the depth-distributed timeseries of ET_j and d_j using Method 3 (minimum drainage). Method 3 is applied beginning with the deepest layer and moving shallower, so a deepest layer needs to be selected before the method is applied. Since transpiration may not occur throughout the full depth of the column, and Method 3 maximizes ET, the choice of maximum depth may affect accuracy of the

mass balance method, which is tested in the synthetic comparison to HYDRUS. To evaluate the impact of choice of maximum depth for the mass balance calculation, we applied Method 3 (minimum drainage) to the Rivendell VMS data using each possible layer shallower than 12 m as the maximum depth. For additional considerations about the effects of data noise, natural variability, and storage capacity assignment on Method 3's field application, see Section S5 in Supporting Information S1.

2.4. Uncertainty and Limitations in Water Content Data

Water content data are essential for any mass balance method in the subsurface, but these type of data can have numerous issues, such as the drift and noise we had to deal with at our site. While it would be valuable to explore the potential impacts of drift and noise on outcomes in a synthetic test, the environment is too idealized to realistically evaluate effects since any drift or noise added could be reversed perfectly. Instead, we consider what the potential impacts may be of incomplete handling of drift and noise in water content data. If sensor drift (rising water content over time) were not removed entirely, then there would be progressively larger storage gains and smaller losses. The overall outcome would be storage accumulation where sensor drift occurs. The opposite would hold if water contents drifted lower, although we did not experience that with our sensors. With rising sensor drift, both ET and drainage fluxes would appear smaller than they should be at the affected layer, which could result in less water available to deeper layers (if drainage is reduced) and could impact mass balance at the deeper layers. This effect, in our modeling strategy, would force precipitation to increase to meet mass balance at the deeper layers so that enough extra precipitation were available to drain deeper during periods of rising storage. During periods of storage loss, this issue would not be apparent. In soil and rock moisture layer depths to 3.64 m, we do see a small effect of storage increases being more likely to be positive when precipitation is adjusted. This same effect could be cause by attributing higher storage to these layers. Regardless, it may be the case that the ET and drainage we report are a little lower than they should be. Falling sensor drift would result in smaller storage gains and larger losses over time, with net loss in storage at the affected layer through time. This would result in larger fluxes of ET and drainage at all times and would be difficult to detect except in the trend of net storage loss, which we do not have in our data. Sensor noise obscures data at fine temporal resolution, and the degree of noise could make it challenging to identify the correct value to use for water content at each timestep. We explored a few different strategies for selecting a daily value from the 15-min data, including: mean daily value, median daily value, and mean with outliers removed. The differences between these different methods were minimal, and uncertainty in means was less than 1% of the value.

2.5. Root Water Uptake Models

Algorithm 2: Algorithm describing the top-down depletion method for the water uptake distribution. $ET_j(t)$ is the ET assigned to layer j at timestep t, $ET_{remaining}(t)$ is the remaining ET demand for timestep t, $ET_{total}(t)$ is the total ET demand for timestep t, $AW_j(t)$ is the available water in storage at layer j for timestep t, $\theta_{j,median}(t)$ is the median water content of layer j over the previous week at timestep t, n is the total number of layers, and $RWU_j(t)$ is the root water uptake for layer j at timestep t.

for each timestep t **do**
  $ET_{remaining}(t) \leftarrow ET_{total}(t)$
  for $j = 1$ to n **do**
    if $\theta_{j,median}(t) \geq 30\%$ **then**
      $ET_j(t) \leftarrow \min(ET_{remaining}(t), AW_j(t))$
    else
      $ET_j(t) \leftarrow \frac{ET_{remaining}(t)}{n-j+1}$
    end if
    $ET_{remaining}(t) \leftarrow ET_{remaining}(t) - ET_j(t)$
    if $ET_{remaining}(t) = 0$ **then**
      break
    end if
  end for
  for $j = 1$ to n **do**

15: $RWU_j(t) \leftarrow \frac{ET_j(t)}{\Sigma_n^{k=1} ET_k(t)}$
16: **end for**
17: **end for**

Using the evapotranspiration curves with depth, we calculated mean water uptake distributions for the full study period and each month of the year during the study period. We then compared these root water uptake distributions to distributions modeled using common formulations listed in Table S5 in Supporting Information S1. Root water uptake is typically modeled as a function of water content, root distribution, a measure of transpiration or PET, pressure heads, and/or soil properties (Kumar et al., 2015). Without soil properties and pressure heads, we are able only to use simplified versions of root water uptake schemes, such as those deployed in ecohydrological models. Here, we apply the four water uptake schemes available as built-in options for the widely used dynamic global vegetation model LPJ-GUESS (Smith et al., 2001) in addition to one scheme we developed based on our conceptual model of the study site (modified top-down depletion, in which storage is generally decreased by evapotranspiration from the top of the profile first, and water uptake extends deeper through dry periods). The four previously published schemes include: rootdist, which models the uptake distribution as the root distribution; wcont, which models the uptake distribution as the water content distribution; rootdist × wcont, which models the uptake distributions as the product of the root distribution and the water content distribution; and drought tolerance = x, which is a modified version of rootdist × wcont that adds an exponent to the water content distribution with value x that simulates more or less tolerance to dry conditions. The top-down depletion method is described in detail below and in Algorithm 1. See Figure S19 in Supporting Information S1 for a visual description of each method. The inputs to the root water uptake models include: water content distribution, root distribution, and (for modified top-down depletion) ET. Water content distribution is calculated at each timestep as the fraction of total water stored during that timestep found in each layer. The root distribution was estimated as the mean uptake distribution over the full study period. The mean uptake distribution approximates an exponentially decreasing function with depth, which is a commonly assumed shape for root distributions. We assumed that the root distribution did not change through time, as is typically the case in ecohydrological models. We then calculated each of the four standard methods from LPJ-GUESS (rootdist, wcont, rootdist × wcont, drought tolerance = x with $x \in (0.1, 1, 2)$) using the mean wcont from the full study period and the mean wcont for each month of the year averaged through the full study period. See Table S5 in Supporting Information S1 for the model equations. The root distribution is used only for three of the root water uptake models from LPJ-GUESS and not incorporated into any of the mass balance calculations or the modified top-down depletion method.

The top-down depletion method needs to be calculated on a daily basis since the method is based on actual volumes of water available in storage and demand for ET rather than distributions. Conceptually, the modified top-down depletion method works by using water higher up in the profile first for ET when it is very wet and spreading water use over a progressively deeper profile as the column starts to dry out. In this way, as upper layers deplete, deeper layers start to be used for ET before the upper layers dry out completely. The process for calculating the root water uptake distribution with the modified top-down depletion method is shown algorithmically in Algorithm 2. The method loops through the layers to assign ET amounts (given the total actual ET observed from the column, known from Method 3 in this case) beginning from the top layer. At each layer, if the median layer water content over the previous week is at least 30%, then as much of the remaining ET as possible will come from that layer. If the median layer water content over the previous week is less than 30%, then the remaining ET demand is divided by the number of layers remaining, including the current layer, and that amount of ET is assigned to the current layer. When top layers are wet, water use will come from near the surface. When the top layers become drier, more ET will come from deeper in the profile. When the full column is drier than 30%, the water uptake distribution is nearly uniform (depending on remaining water available at each layer). The threshold of 30% was selected to represent a dry condition but not fully dry. If the threshold is increased, then water uptake spreads to deeper layers at higher remaining water contents. If the threshold is decreased, more water use is concentrated shallower in the profile until the top layers reach lower water contents. The choice of a wetness threshold in this scheme is the only user-defined parameter, whereas most of the other methods require a root distribution, which is more difficult to constrain. After ET is assigned to a layer, the remaining ET demand is updated to remove the ET assigned to that layer. If there is no ET left, or the bottom of the profile is reached, the method is finished. The end result is a vertical distribution of ET with a total amount that matches the ET demand for that timestep. A root water uptake profile is found by normalizing the ET distribution for each timestep. Then,

the daily distributions are averaged over the full study period or for each calendar month averaged over the full study period for comparison with the other root water uptake distribution methods.

3. Results

3.1. Method 3 (Minimum Drainage) Performs Best for Calculating Depth-Distributed Timeseries

Synthetic tests using HYDRUS are shown at 25 cm vertical resolution. Across all climate locations shown in Figure 5a, Method 3 outperforms Methods 1 and 2 at simulating depth-distributed ET and drainage fluxes. See Figure S2 in Supporting Information S1 for details of performance across climate types. Detailed performance is shown in the main text only for the synthetic test based on the Rivendell site. Methods 2 (power law drainage) and 3 (minimum drainage) perform similarly at simulating the total ET timeseries produced by HYDRUS, while Method 1 (dry periods only) performs less well (Figures 3a–3c). However, Method 2 (power law drainage) is calibrated to maximize performance on total ET. For all methods, total ET generally increases with increasing maximum depth (Figure 3b, Figure S2 in Supporting Information S1 with variation among climate types). Method 3 total ET stabilizes at a maximum depth equal to the total ET from HYDRUS, shown as a dotted line, where it remains as maximum depth increases above about 500 cm. This behavior is consistent with additional deeper ET nodes adding to the total as depth is increased. Since HYDRUS ET stops at a depth of 6 m, and the amount of ET between 5 and 6 m is relatively small, the total ET is reached around that depth, and no additional ET is added at progressively deeper depths. Methods 1 and 2 are not sensitive to the maximum ET depth in HYDRUS and continue adding more ET as maximum depth increases.

Mass balance error for Methods 1 and 2 increases with maximum depth (Figure 3d). For Method 1 (dry periods only), this is because there are additional layers that can have positive storage changes (resulting in negative estimated ET), but additional layers do not reduce error for layers above. For Method 2 (power law drainage), the reason is similar–more opportunities for modeled drainage to result in mass balance violations without any opportunities to improve errors from above. Even when defined, Method 1 (dry periods only) performance is clearly poorer than Methods 2 and 3, but the performance is even worse given that Method 1 produces output for only 54% of the time period (Figure 3d), missing the wettest (and perhaps most difficult to simulate) parts of the timeseries. Considering Figures 4a and 4b comparing calculated total ET timeseries to the actual timeseries from HYDRUS, it is clear that Method 1 (dry periods only) is less effective than Methods 2 and 3. Method 1 (dry periods only) significantly overpredicts ET during some timesteps and provides no ET estimate for nearly half of the timeseries. Methods 2 and 3 both look very good when compared to total ET (except during late winter for Method 2 and at the end of fall for Methods 2 and 3). These performance patterns are similarly clear in the scatter plot in Figure 4c, which shows that all points fall near the 1-1 line for Methods 2 and 3, but Method 1 points can fall far to the right of the line, indicating overpredicted total ET.

While Method 2 (power law drainage) and Method 3 (minimum drainage) appear to perform similarly well for total ET, Method 3 (minimum drainage) performs best at simulating depth-distributed ET and drainage timeseries (Figures 3e–3h). Method 3 (minimum drainage) has the highest KGE (Figures 3e and 3g) and lowest MAE (Figures 3f and 3h) for both ET and drainage depth-distributed timeseries, except for shallow node depths when Method 1 (dry periods only) has lower MAE for drainage. As with total ET, however, Method 1 (dry periods only) is missing 45% of the timeseries, so the low MAE values are skewed since time periods with significant drainage are missing from the timeseries. Importantly, Method 3 (minimum drainage) is the only method for which MAE for ET is less than ET (Figure 3f). MAE tends to reduce with depth for both depth-distributed ET and drainage (except for Method 1 (dry periods only) with drainage) since magnitudes are smaller at depth. For Method 1 (dry periods only), drainage MAE increases with depth since drainage is more delayed from precipitation, meaning that larger drainage magnitudes can happen at deeper depths further in time from precipitation events.

The superior performance of Method 3 (minimum drainage) is visually apparent from the timeseries of depth-distributed ET and drainage (Figures 4d–4o). Generally, Method 1 (dry periods only) does a decent job most of the time when it is defined but can significantly overestimate ET during wet times of year and occasionally result in negative ET. Method 2 (power law drainage) produces similarly poor results for depth-distributed ET with some overly positive and highly negative ET values. Method 3 (minimum drainage) generally matches the ET pattern well with interpolated lines through the wettest periods so that some peaks and dips are flattened. This cumulative sums of the fluxes in the center column (Figures 4e and 4h) show by far the closest match for Method

10.1029/2025WR040778

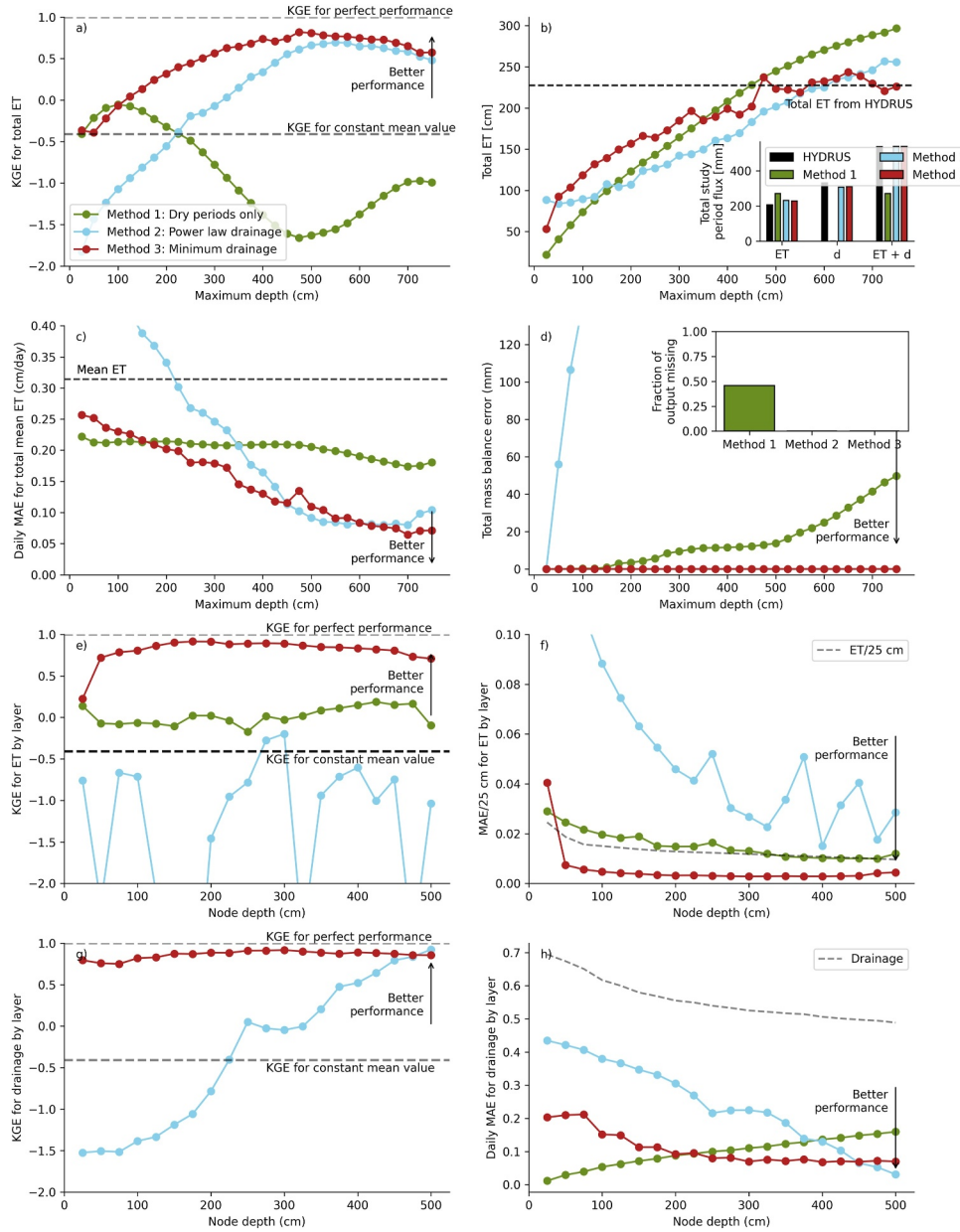

Figure 3. (a, c, d) Performance metrics (relative to HYDRUS simulations) for each method on overall timeseries as a function of maximum node depth. The inset in panel (b) shows total fluxes over the study period, and in panel (d) shows fraction of missing output for each method. No output is missing for Methods 2 and 3. Panel (b) complements panel (a) by showing the total ET as calculated by each method with each maximum node depth. (e–h) Performance metrics for each method as measured on depth-distributed time series as a function of node depth. In panels (e) and (g), KGE values for some depths for Method 1 can be very negative. Panels (e–h) are shown with a depth resolution of 25 cm and a maximum depth of 500 cm.

3, although compensating errors for Method 2 result in a cumulative timeseries that approximates the HYDRUS ET at 50–75 cm decently well. The scatter plots in Figure 4f and i show that Method 3 depth-distributed ET generally falls near the 1-1 line, whereas the points from the other methods can fall very far off the 1-1 line and even outside the plot bounds.

Method 1 (dry periods only) always predicts 0 drainage, which is frequently correct when it is defined but not always, particularly during very wet periods. Method 2 (power law drainage) tends to underpredict drainage but get the pattern right. Method 2 (power law drainage) would likely perform better if a different power law parameter were trained for each depth (suggested by the clear offset from the 1-1 line in Figures 4i and 4o), but

10.1029/2025WR040778

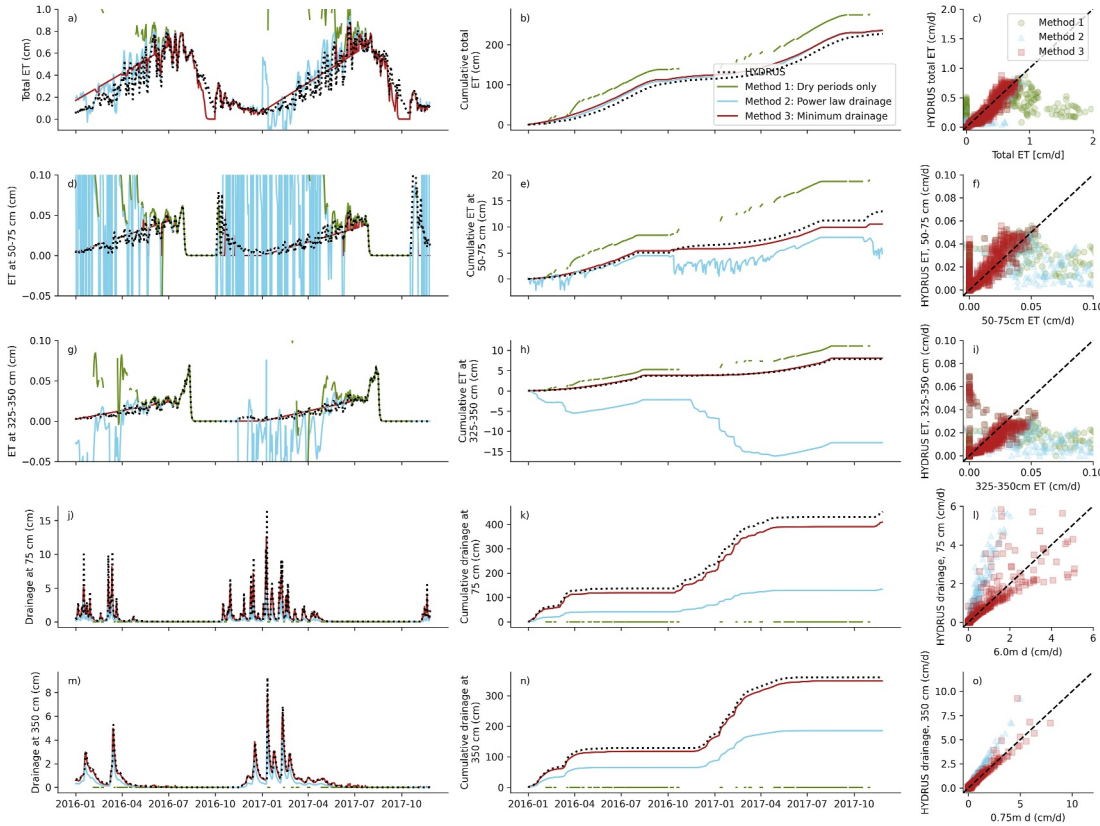

Figure 4. Sample timeseries using each of the three methods for total ET from the column (a), ET at (d) 50–75 cm depth and (g) 325–350 cm depth, and drainage at (j) 75 cm depth and (m) 350 cm depth. Cumulative curves for each are shown in the center column (b, c, e, h, k, n), and scatter plots of daily values on the right (c, f, i, l, o). The first two columns follow the legend in panel (b), and the right column follows the legend in panel (c). All methods are run using 25 cm node spacing and a maximum depth of 500 cm. Panels (a), (d), (f), (g), and (i) are clipped to improve visibility of data. Errors for Methods 2 and 3 can be an order of magnitude larger.

that would not generally be possible with field data collection methods, and a real field site may be more likely to deviate from power law behavior than HYDRUS outputs. Method 3 (minimum drainage) generally matches the drainage magnitude and shape extremely well.

Of the three methods, Method 3 (minimum drainage) is the only method capable of producing reasonable depth-distributed ET timeseries. From the center column of Figure 4 and second column of Figure S2 in Supporting Information S1, it is clear that the magnitude and timing of ET and drainage are well represented by Method 3. Method 2 does a decent job with the timing of drainage but not as well with the magnitude (panels k and n). Only Method 3 can reproduce timing and magnitude of ET. While only two layer depths are shown in Figure 4, performance for other layer depths is very similar (see Figures S7–S10 in Supporting Information S1). The only exception is the 25 cm layer depth, for which ET is significantly overpredicted using Method 3. Using a lower vertical resolution, though, (50 or 100 cm node spacing) avoids this issue, which is specifically related to the very shallow surface. Performance for the upper soil layer for 50 and 100 cm resolution is similarly good to other layers. Depths of poorer performance varies among climate types (Figure S2 in Supporting Information S1). For climate types with overall good performance (Bsk, Bwh, Csa, Csb), poorer performance is always among the shallow layers. For the Mediterranean climates (Csa, Csb), the poorest performance is for the shallowest layer. For the more arid climates (Bsk, Bwh), performance is less good below a depth of about 1 m but still overall excellent. For other climate types (Aw, Cfa, Cfb, Dfa, Dfb), performance varies more with depth.

Method 3 performs well against total ET compared to the best methods tested by Guderle and Hildebrandt (2015) when using the lowest resolution (daily for inverse modeling, 12 hr for daily fluctuation method of Li et al. (2002)). In terms of correlation coefficient (perfect performance $R = 1$), Method 3 performance for the synthetic Rivendell test is $R = 0.78$, while the inverse modeling approach tested by Guderle and

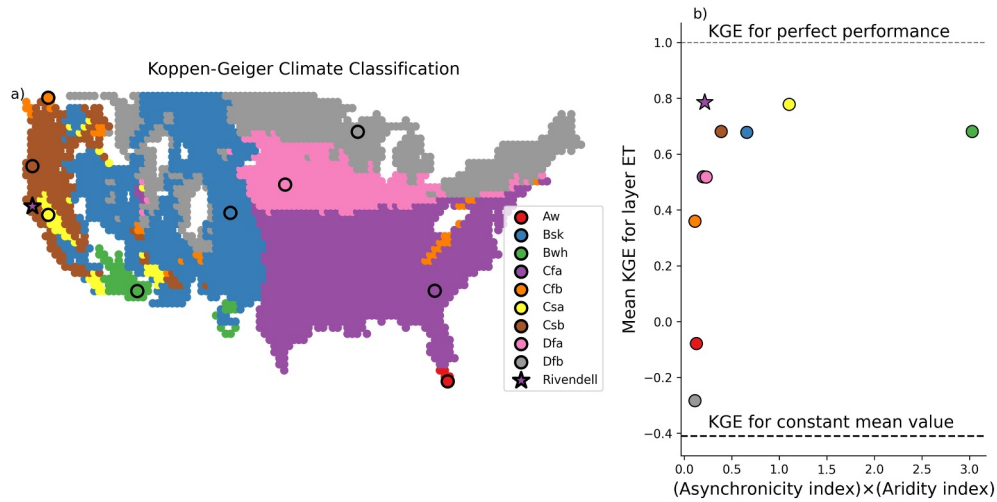

Figure 5. (a) Map of the Conterminous United States with the most common Koppen-Geiger climate types marked, key given in Table S3 in Supporting Information S1. Circles are the locations used for the synthetic HYDRUS test (more information on sites in Table S3 in Supporting Information S1), and the star marks the study location. (b) Method 3 performance improves as rainfall seasonality or aridity increase.

Hildebrandt (2015) has $R = 0.99$, and the subdaily variation approach of Li et al. (2002) has $R = 0.85$. Method 3 relative variance (perfect performance $RV = 1$) is $RV = 0.82$, compared to the inverse modeling approach with $RV = 1.11$ and the daily fluctuation approach has $RV = 4.22$. In terms of bias (perfect performance 0%), Method 3 performance is 7%, inverse modeling approach is 0.89%, and the daily fluctuation approach is 202.9%.

3.2. Method 3 (Minimum Drainage) Is Applicable Across the Western US

While Method 3 outperforms the other mass balance methods at simulating depth-distributed RWU and drainage for all climate types, overall performance varies among the climate types (Figure S2 in Supporting Information S1). In general, performance at simulating depth-distributed ET improves if Aridity Index or Asynchronicity Index are larger (Figure 5b). This aligns well with how the method is designed since ET is approximated by a linear interpolation during wet periods. As a result, climates with fewer wet periods or with most ET occurring during dry periods are most appropriate for application of Method 3. Figure 5a shows that these climates (Bwh, Csa, Bsk, Csa) cover most of the Western US.

3.3. ET Patterns Modeled in Field Application Compare Well to Independent ET Data Sets

Given the superior performance of Method 3 (Minimum drainage), we applied this method to the VMS data from the Rivendell field site, and all remaining results refer to the ET and drainage timeseries resulting from this process. Using the Rivendell field data, there is a soil layer and 7 VMS layers at about 1.5 m vertical resolution to a depth of about 12 m. We compare ET estimates using Method 3 to a basin-wide mass balance for the study area (drains to Elder Creek, U.S. Geological Survey, 2021), the distributed ET product PML-V2 (Y. Zhang et al., 2016; Y. Zhang et al., 2019; F. Zhang & Zhang, 2021), and qualitative water uptake patterns from sapflow data (Link et al., 2014). The basin-wide mass balance results in 599–666 mm/yr of ET for water years 2016–2019, and PML-V2 indicates 566–604 mm/yr. These estimates align well with one another and are comparable to or up to 100 mm greater than the Method 3 annual ET of 508–591 mm/yr. Method 3 drainage is 299–370 mm/yr greater than streamflow (1,865–1,912 mm/yr), with most of the difference during the wet season. During the dry season, streamflow exceeds drainage calculated from Method 3 (see Text S7 in Supporting Information S1 for more details). Since ET is well-matched throughout the year (see comparison to PML-V2 ET and sapflow in Figure S17 in Supporting Information S1), the additional drainage may be explained by additional water use from groundwater before it reaches the stream, additional interception losses not properly accounted for, errors in water content data that forced additional precipitation with Method 3 (water year increase of 135–332 mm), or relatively lower water use at the VMS site since Rivendell is on a north-facing slope. For more details and visual representation, see Text S6 in Supporting Information S1.

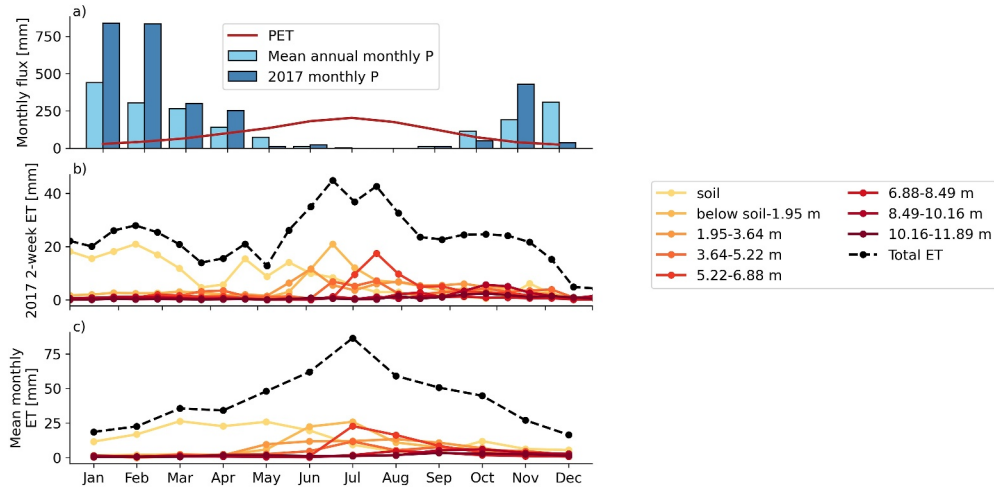

Figure 6. (a) Monthly precipitation patterns at Rivendell for the full period (January 2016–December 2019): averages (light blue), example year 2017 (dark blue), and PET (red). Calculated ET timeseries for each depth using Method 3 (Minimum drainage) for (b) 2017 and (c) mean over the study period. Colored lines indicate ET from each VMS layer, and the black dashed line indicates total column ET.

3.4. ET Withdraws Deeper Storage Later in the Dry Season

The total ET timeseries at Rivendell modeled using Method 3 (black dashed line, Figures 6b and 6c) reaches its peak in the same month as PET (red line in Figure 6a). Soil ET is activated early in the wet season, and rock moisture layers activate once the subsurface begins to dry out (Figure 6c for full study period and Figure 6b for 2017). This pattern results in a water uptake profile that primarily comes from soil during the wet season (Figures 7c–7h). By the end of the dry season (September), water contributions from all depths are similar (Figure 7m). Water usage shifts toward shallow depths again as the rain starts in October (Figure 7b), in line with observations from sapflow (Link et al., 2014). Over the course of a water year, 193 mm (36%) of ET comes from the soil, and the remaining ET is distributed through rock moisture (347 mm, 64% ET) with approximately decreasing ET with depth (Figure 7a). ET from soil far exceeds the soil storage capacity since soil water storage is used and recharged multiple times throughout the wet season, whereas rock moisture water use is very close to the storage capacity.

3.5. ET Magnitude and Seasonality From Rock Moisture Consistent Every Year

Amounts of ET from each of the port depths are very similar annually across all years in all layers except for the soil (Figure 8a). The primary difference in precipitation delivery between 2017 and the other water years included in the study period occurred during the wettest time of year (October–January, Figure 8b). During this period, there was substantially more soil ET in the wettest year (2017) than in the other two water years, but water use from other depths was not significantly different between water years and did not follow a pattern that accords with the difference in precipitation. The difference between 2019 and 2018 was during the period from February-May (Figure 8c). Despite this, there are very minimal differences in soil ET between years during any other time of year. As a result, the seasonal differences in soil water use result in much higher soil ET during the year with the wet October–January than either other year. The relative distribution of soil water use between seasons is impacted by choice of soil moisture probe (Text S7 in Supporting Information S1), so these results may not be representative of the full landscape. However, water year water use is generally consistent among soil moisture probes (water year results generally within 20% of results using mean across soil moisture probes regardless of soil moisture probe used, Text S7 in Supporting Information S1). Rock moisture water use is very minimal from October–May but becomes important in June–September. In August-September, only 7–9 mm ET comes from soil, and the remaining 93–115 mm comes from rock moisture. Overall, these findings indicate consistent water use from rock moisture each year but greater potential for soil water use during the early wet season based on precipitation delivery.

10.1029/2025WR040778

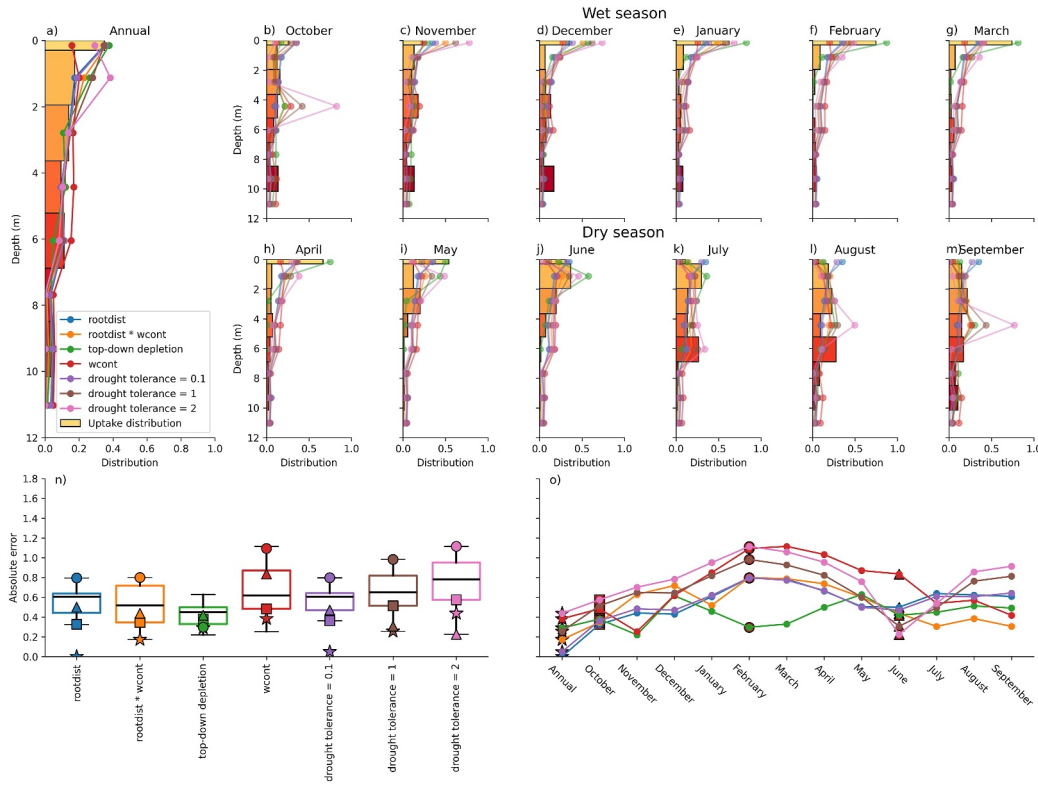

Figure 7. Mean annual (a) and mean monthly (b–m) root water uptake distributions throughout the study period. The colored lines indicate modeled uptake distributions using 6 methods found in popular dynamic vegetation models and one method (modified top-down depletion) introduced here. See Section 2.5 for a description of each method. Panel (n) shows the overall performance of each method in terms of absolute error in the distribution, and (o) across each uptake distribution. The colors across all panels match the legend in (a), and the markers in panel (n) represent the data points of the same symbol and color in panel (o). For example, square markers indicate October model fits. In panels (a–m), the shallowest layer is soil.

3.6. Some Deep Drainage Continues Late in the Summer

Drainage decreases with depth (Figure 9a) since some water is held in tension at each depth (to later be used for ET) rather than draining deeper. Drainage timeseries look very much like precipitation (Figures 9b–9i, solid lines), with magnitude decreasing with depth. To better visualize drainage that continues during the dry season, we also plot drainage on non-raining days (dotted black lines in Figures 9c–9i). Looking at these curves, drainage shifts later in time at deeper depths. With the smaller vertical scale, it also becomes clear that drainage continues at deeper depths well into the dry summer. These observations align well with when water samples were drawn from each depth (shaded regions in Figures 9c–9i), which indicates that water was available for drainage. Generally, the shaded regions start after less than 10 mm of drainage is indicated by Method 3 at a given depth, and drainage becomes negligible at the end of each year when the shading stops (easier to see on dotted lines). This agreement between the shaded regions and the drainage timeseries provides an independent line of evidence supporting the realism of the produced drainage and ET timeseries. Drainage from all depths follows a similar, close pattern in all months except July and August, when the shallowest depth have much less drainage. These are the only 2 months with 0 mm average precipitation during the study period. It may be that the extended period with no rainfall causes the shallow layers to dry out sufficiently that drainage reduces relative to deeper layers that may experience less root water uptake and continue to receive a small amount of drainage from above.

3.7. Root Water Uptake Distributions Are Highly Seasonal

All water uptake distribution models except the modified top-down depletion model perform best from June–September with poorer performance from January–May (Figure 7o). The modified top-down depletion method performs similarly to the other method in May–December but significantly better in February-April, covering most of the period when soil water use is important. Of all of the methods tested, the best performance overall

10.1029/2025WR040778

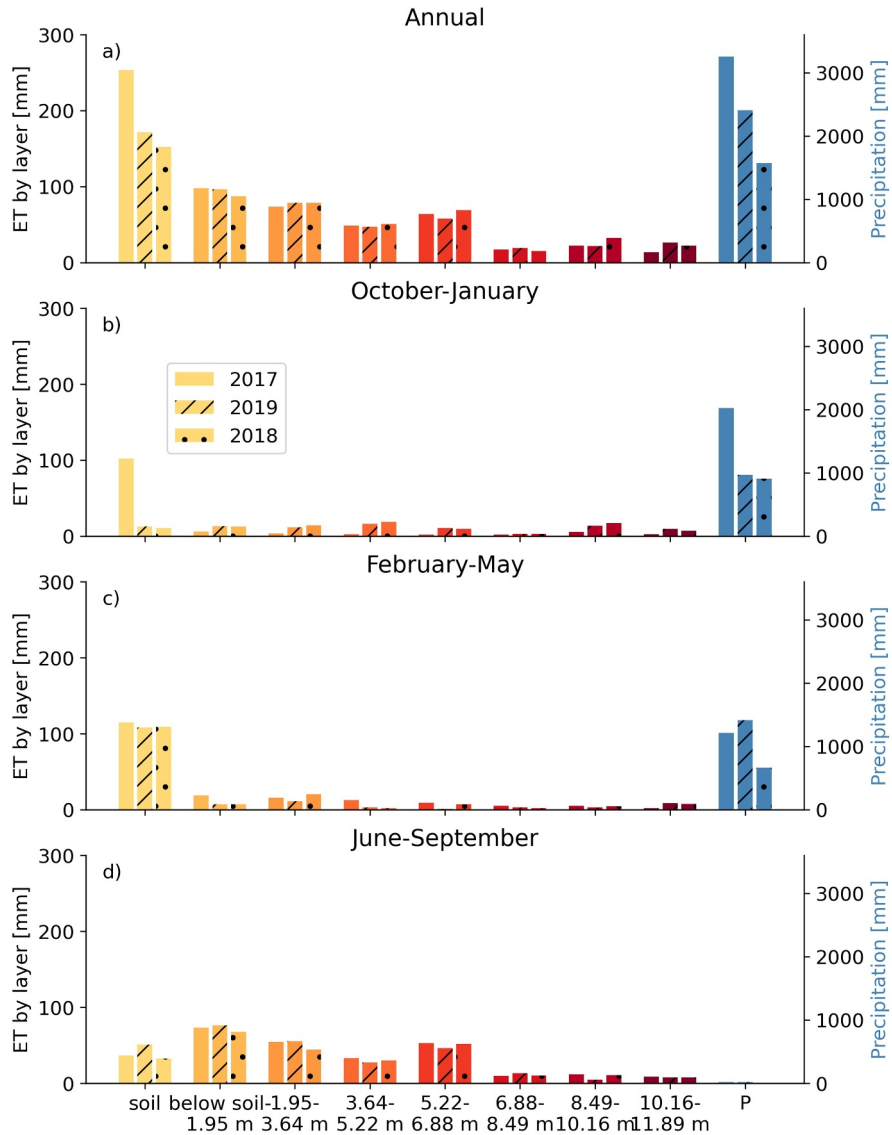

Figure 8. (a) Water year and (b–d) seasonal ET and precipitation totals for each year in the study period. Precipitation is outlined in black and follows the *y*-axis on the righthand side. The bar color indicates the water year, as indicated in the legend in panel (b). The *x*-axis indicates the VMS layer, including soil and each of the VMS ports to a depth of about 12 m.

throughout the year is shown by the top-down depletion method (Figure 7n), which captures the importance of soil water in the wet season and the nearly uniform water uptake distribution late in the dry season.

4. Discussion

The mass balance method presented in this study (Method 3: minimum drainage method) performs well at capturing depth-distributed evapotranspiration (ET) and drainage in a synthetic test using HYDRUS model outputs and precipitation inputs (Figures 3 and 4). This good performance holds across Mediterranean and desert climate types found across the Western United States and including the study site (Rivendell). Additionally, the total column ET timeseries modeled for Rivendell is consistent with detailed studies of hydrological fluxes at this site. Our results agree with prior findings that water use from weathered bedrock is an essential resource for plants, and that transpiration is sourced progressively deeper later in the dry season (Rempe & Dietrich, 2018). Further, our finding that summer rock moisture ET is very consistent between years aligns well with the designation of Rivendell as a storage capacity-limited site (Hahm et al., 2019). In this framework, water available

10.1029/2025WR040778

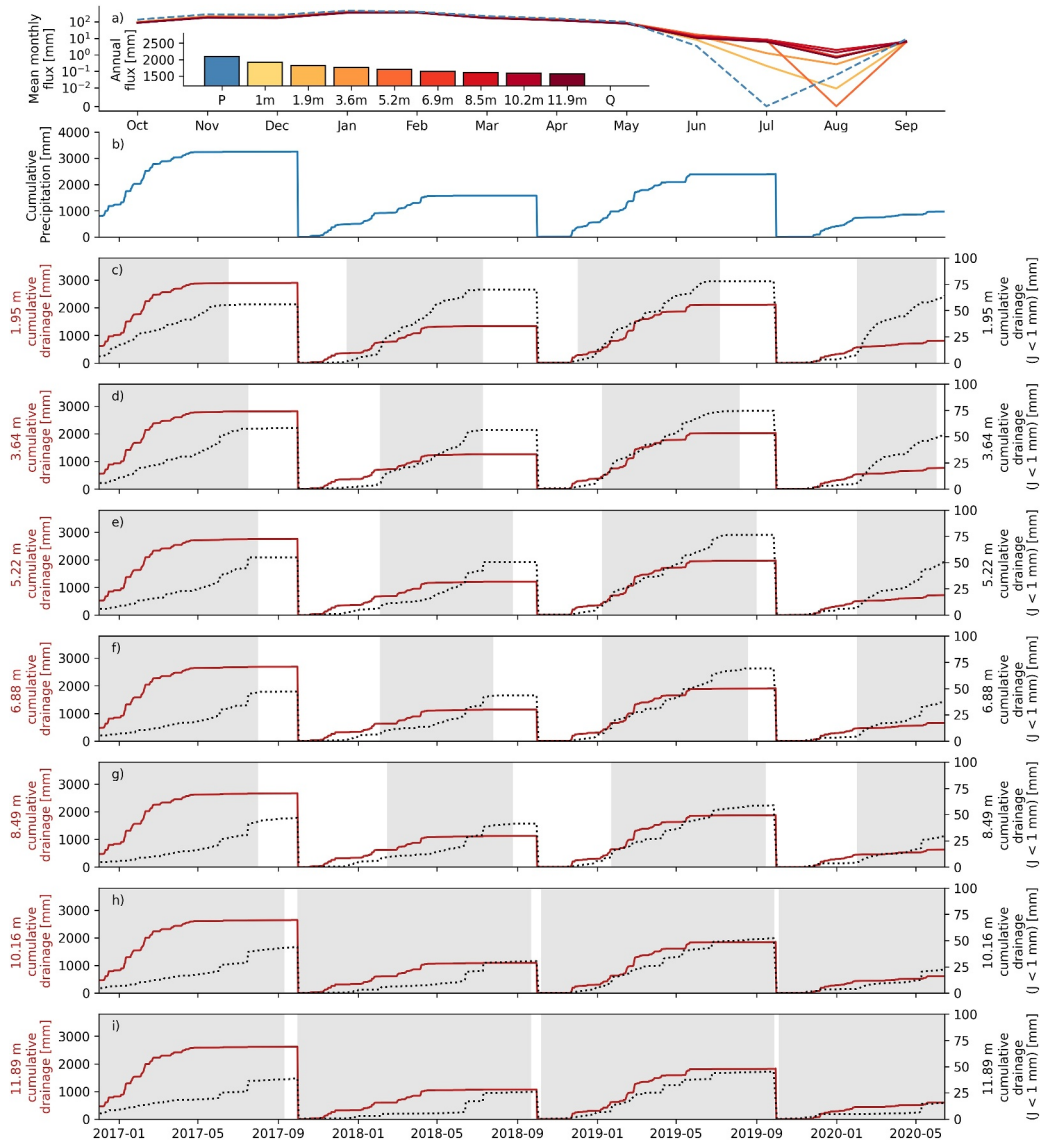

Figure 9. Modeled drainage fluxes at Rivendell. (a) Mean monthly (annual in inset) drainage and precipitation at each node depth. (b–i) shows modeled drainage at each VMS depth below soil throughout the study period. Solid red lines are cumulative drainage for all days (left *y*-axis), and the dotted black lines are the cumulative drainage for days with no precipitation (right *y*-axis). Shaded regions are periods during which water samples were drawn from that depth, indicative of relatively low tension pressure heads consistent with likely drainage during that period.

to plants is limited by the subsurface storage capacity rather than annual precipitation, meaning that plants experience essentially the same rock moisture water availability in both wet and dry years. These conditions result in consistent dry season water use between years that does not depend on annual precipitation, which closely aligns with our finding of similar summer water use patterns with depth for each water year in the study despite large differences in annual precipitation. Differences in annual precipitation translate only to differences in soil water use between years, which manifest during the wet season. These consistencies support the use of this mass balance method for producing data-driven timeseries of ET and drainage.

4.1. Plant Water Source Identification Using Isotopes

The uptake distributions in Figure 7 show distinct seasonal changes in water sources for plants. In January–April, nearly all water uptake comes from the soil. Moving into the late summer, the uptake distribution flattens out so that water is used nearly equally from all depths during that period. As a result, sampled xylem water in January–

April should look very similar to plant available soil water, and sampled xylem water in August-September should be an even mix of waters seasonally stored throughout the vadose zone. Our observations indicate that water stored below soil accounts for 64% of annual water uptake. In summer months (June–September), 85% of water uptake comes from below soil on average. This dynamic is similar to the observations of Rempe and Dietrich (2018), Hahm et al. (2020), and Rose et al. (2003), who found that water use moved shallow during the wet winter months and extended deeper as the dry season progressed. These findings indicate that studies seeking to identify water sources used by plants in seasonally dry forests must take into account possible water sources in weathered bedrock in addition to soil and groundwater, which is consistent with findings from other isotope studies that water stored in weathered bedrock is an important water source (Liu et al., 2014; Querejeta et al., 2006).

The minimum drainage method (Method 3) presented in this study provides an independent means to identify water sources for plant water use that can be used to verify water sources inferred from isotopic data where depth-distributed moisture data are available. This method can also provide greater depth resolution than isotopic data since pore waters stored in the vadose zone may be well-mixed, with water from distinct depths indistinguishable. Pairing these methods together could allow for stronger interpretation of the seasonality of plant water sources.

4.2. Root Zone Water Storage and Baseflow

Our findings indicate that deep drainage (drainage from the bottom of the VMS profile) from the root zone continues into the dry season. This drainage can be thought of as groundwater recharge since the water table extends nearly up to the deepest sensor depth used for analysis. This summer recharge may be important for sustaining streamflow through the dry season, depending on whether recharge volumes are great enough to result in important head gradient changes, and transit times to the stream are fast enough during the dry summer months to propagate this change to the stream. We were unable to associate modeled summer drainage patterns with recession behavior in nearby wells due to measurement limitations compounded with uncertainty in model outputs. However, it remains to be explored whether this summer recharge may be important for streamflow. If so, this finding indicates that summer recharge, and thus streamflow, may be vulnerable to changes in ET magnitude or shifts in species composition (Link et al., 2014). However, the ET timeseries calculated in this study represents water uptake from all plants near to sensor locations on the hillslope, providing an integrated description of plant water uptake for the plant community, rather than attributing water withdrawals to particular individuals or species.

The method presented in this study provides a way to infer the seasonal dynamics of recharge on hillslopes, which remains very difficult to quantify (Dralle et al., 2023). When combined with daily-resolution water content observations at disparate sites, the resulting drainage timeseries may lead to insights on how distinct plant communities and climates result in different magnitudes and seasonalities of recharge. The methods developed in this study would allow for observations in changes in water uptake with different management actions, giving real-time feedback on how different actions impact recharge directly.

4.3. Modeling Uptake Distributions

The findings of this study show water uptake distributions throughout the year. When possible, plants tend to use the shallow water, which aligns with the finding that root density is highest near the surface (Schenk & Jackson, 2002). Shallow water uptake, when possible, is theoretically favored since maintaining root architecture and uptake of resources from shallow depths requires less energy (Adiku et al., 2000), nutrients are more available (Jobbagy & Jackson, 2001), and shallow depths are less likely to be oxygen deficient (Hillel, 2003). Previous isotopic studies have identified similar water uptake patterns, with soil the predominant water source in wet periods and progressively deeper sources during dry growing periods (Asbjornsen et al., 2008; Dai et al., 2015; McCole & Stern, 2007; Rose et al., 2003; Song et al., 2014). Our findings may exaggerate soil water use since soil evaporation is lumped with root water uptake, but the patterns broadly match prior work. Rose et al. (2003) suggest that this behavior shows a switch between uptake distributions that more closely match the rooting distribution during wet periods and uptake distributions that follow water availability in dry periods. We found that the root distribution performs well in wet periods. In dry periods, the water content distribution does not dictate the water uptake distribution, but water content-based distributions performed well during the summer, and the rootdist × wcont method (multiplying distribution of roots and water content for each month) was the

highest-performing or second-best-performing method for the entire water year except for October–December and April–May. These findings demonstrate that models based on root distribution and water content distribution alone may not be adequate to capture the seasonal changes in water uptake distribution since the poorer performance occurs specifically during seasonal shifts. The modified top-down depletion method presented here is better able to capture the seasonal shift but still performs imperfectly in the transition from the wet to the dry season. An advantage of the modified top-down depletion method is that it does not require a root distribution, which is rarely known in practice. Future work could explore implementing more complex water uptake strategies into ecohydrological models and studying changes in uptake strategy as water availability changes. It may improve their ability to capture seasonal differences in subsurface chemical processes and ET.

4.4. High Temporal Resolution Needed for Weathered Bedrock Vadose Zone Observations

This study provides the first observation-based depth-resolved evapotranspiration (ET) timeseries in high temporal resolution throughout soil and deep into weathered bedrock. The observation of significant water use below soils is consistent with understanding of the Rivendell site (Rempe & Dietrich, 2018). However, this phenomenon is not unique to Rivendell; the importance of water stored in weathered bedrock for plant water use is now well recognized in the hydrological community (e.g., Ehlert et al., 2024; Hahm et al., 2020, 2022; Maysonnave et al., 2022; McCormick et al., 2021 Rempe & Dietrich, 2018; Rose et al., 2003; Ruiz et al., 2010; Schwinning, 2010). Accurately capturing the amount of water available to plants improves our ability to model plant water use, plant community composition, and carbon cycle dynamics (Lapides et al., 2023). The dynamics of plant water uptake and root distributions are still difficult to capture due to limited observations globally. Daily resolution water content data at distributed depths throughout the weathered bedrock vadose zone in particular are extremely rare, and the mass balance technique presented in this study requires daily data; performance drops rapidly if temporal resolution is coarser (S6). The importance of water stored in weathered bedrock and the as-yet limited knowledge of the drivers of water use and storage dynamics at depth motivate increased observation of the deep weathered bedrock vadose zone at disparate sites and with enhanced temporal resolution.

5. Conclusions

In this study, we developed a new data-driven mass balance technique for calculating depth-distributed evapotranspiration (ET) and drainage fluxes and applied this method to a unique set of observational data at an intensively monitored site in Northern California (Rivendell). By comparing the results of our mass balance technique to 1-D simulations in HYDRUS, we found that the newly presented technique is the only data-driven (i.e., no process assumptions are made) method in the literature that is capable of reproducing depth-distributed ET (including soil evaporation and root water uptake, RWU) and drainage patterns from daily storage changes with no additional process assumptions. Our findings show that this technique is broadly applicable across arid and Mediterranean regions. Rivendell was an ideal location to apply this new mass balance method since there is a history of depth-distributed water content measurements at a set of boreholes in addition to a Vadose-zone Monitoring System (VMS) that records water content at high temporal resolution throughout the vadose zone down to 16.5 m depth. Our results show daily timeseries of root water uptake by layer to a depth of 11.86 m. From these timeseries, we see that water use spreads deeper into the profile as the dry season progresses, and most water use is from the soil during the wettest period. These timeseries can be converted into water uptake distributions that vary throughout the year, indicating a strong seasonal pattern in water uptake with shallow water use in January–April and water use that becomes more evenly distributed with depth by August. Drainage timeseries show that deep drainage continues long into the dry season, suggesting that recharge from the vadose zone could impact summer streamflow. These findings highlight the importance of water availability for driving root water uptake patterns and identifies ongoing deep drainage through the dry season. These findings motivate further daily-resolution observations of hydrological and biogeochemical phenomena into the deep vadose zone.

Conflict of Interest

The authors declare no conflicts of interest relevant to this study.

Data Availability Statement

Supplementary code and data for this work are published at https://github.com/lapidesd/ET_layers/blob/main (Lapides et al., 2024).

Acknowledgments
We acknowledge funding from NSF EAR Award 2100760, an NSERC Discovery award, a Canadian Foundation for Innovation JELF award, and support from the Angelo Coast Range Reserve and University of California Reserve System.

References

Abatzoglou, J. T. (2013). Development of gridded surface meteorological data for ecological applications and modelling. *International Journal of Climatology*, *33*(1), 121–131. https://doi.org/10.1002/joc.3413

Adiku, S., Rose, C., Braddock, R., & Ozier-Lafontaine, H. (2000). On the simulation of root water extraction: Examination of a minimum energy hypothesis. *Soil Science*, *165*(3), 226–236. https://doi.org/10.1097/00010694-200003000-00005

Asbjornsen, H., Shepherd, G., Helmers, M., & Mora, G. (2008). Seasonal patterns in depth of water uptake under contrasting annual and perennial systems in the corn belt region of the Midwestern US. *Plant and Soil*, *308*(1–2), 69–92. https://doi.org/10.1007/s11104-008-9607-3

Bachofen, C., Tumber-Dávila, S. J., Mackay, D. S., McDowell, N. G., Carminati, A., Klein, T., et al. (2024). Tree water uptake patterns across the globe. *New Phytologist*, *242*(5), 1891–1910. https://doi.org/10.1111/nph.19762

Berghuijs, W. R., Luijendijk, E., Moeck, C., van der Velde, Y., & Allen, S. T. (2022). Global recharge data set indicates strengthened groundwater connection to surface fluxes. *Geophysical Research Letters*, *49*(23), e2022GL099010. https://doi.org/10.1029/2022gl099010

Bilir, T. E., Fung, I., & Dawson, T. E. (2021). Slope-aspect induced climate differences influence how water is exchanged between the land and atmosphere. *Journal of Geophysical Research: Biogeosciences*, *126*(5), e2020JG006027. https://doi.org/10.1029/2020jg006027

Breña Naranjo, J., Weiler, M., & Stahl, K. (2011). Sensitivity of a data-driven soil water balance model to estimate summer evapotranspiration along a forest chronosequence. *Hydrology and Earth System Sciences*, *15*(11), 3461–3473. https://doi.org/10.5194/hess-15-3461-2011

Brocca, L., Moramarco, T., Melone, F., & Wagner, W. (2013). A new method for rainfall estimation through soil moisture observations. *Geophysical Research Letters*, *40*(5), 853–858. https://doi.org/10.1002/grl.50173

Cauteruccio, A., Colli, M., Stagnaro, M., Lanza, L. G., & Vuerich, E. (2021). In-situ precipitation measurements. In *Springer handbook of atmospheric measurements* (pp. 359–400). Springer.

Chai, Y., Liu, H., Yu, Y., Yang, Q., Zhang, X., Zhao, W., et al. (2023). Strategies of parameter optimization and soil moisture sensor deployment for accurate estimation of evapotranspiration through a data-driven method. *Agricultural and Forest Meteorology*, *331*, 109354. https://doi.org/10.1016/j.agrformet.2023.109354

Dahan, O., Talby, R., Yechieli, Y., Adar, E., Lazarovitch, N., & Enzel, Y. (2009). In situ monitoring of water percolation and solute transport using a vadose zone monitoring system. *Vadose Zone Journal*, *8*(4), 916–925. https://doi.org/10.2136/vzj2008.0134

Dai, Y., Zheng, X.-J., Tang, L.-S., & Li, Y. (2015). Stable oxygen isotopes reveal distinct water use patterns of two haloxylon species in the gurbantonggut desert. *Plant and Soil*, *389*(1–2), 73–87. https://doi.org/10.1007/s11104-014-2342-z

Dingman, S. L. (2015). *Physical hydrology*. Waveland press.

Dontsova, K., Balogh-Brunstad, Z., & Chorover, J. (2020). Plants as drivers of rock weathering. *Biogeochemical cycles: Ecological drivers and environmental impact*, 33–58. https://doi.org/10.1002/9781119413332.ch2

Dralle, D. N., Hahm, W. J., & Rempe, D. (2023). Inferring hillslope groundwater recharge ratios from the storage-discharge relation. *Geophysical Research Letters*, *50*(14), e2023GL104255. https://doi.org/10.1029/2023gl104255

Dralle, D. N., Hahm, W. J., Rempe, D. M., Karst, N. J., Thompson, S. E., & Dietrich, W. E. (2018). Quantification of the seasonal hillslope water storage that does not drive streamflow. *Hydrological Processes*, *32*(13), 1978–1992. https://doi.org/10.1002/hyp.11627

Ehlert, R. S., Hahm, W. J., Dralle, D. N., Rempe, D. M., & Allen, D. M. (2024). Bedrock controls on water and energy partitioning. *Water Resources Research*, *60*(8), e2023WR036719. https://doi.org/10.1029/2023wr036719

Esfahani, M. N., & Sonnewald, U. (2024). Unlocking dynamic root phenotypes for simultaneous enhancement of water and phosphorus uptake. *Plant Physiology and Biochemistry*, *207*, 108386. https://doi.org/10.1016/j.plaphy.2024.108386

Famiglietti, J., & Wood, E. F. (1994). Multiscale modeling of spatially variable water and energy balance processes. *Water Resources Research*, *30*(11), 3061–3078. https://doi.org/10.1029/94wr01498

Feddes, R., Kowalik, P., & Zaradny, H. (1978). Water uptake by plant roots. *Simulation of field water use and crop yield*, 16–30.

Flint, A. L., Flint, L. E., Kwicklis, E. M., Fabryka-Martin, J. T., & Bodvarsson, G. S. (2002). Estimating recharge at yucca Mountain, Nevada, usa: Comparison of methods. *Hydrogeology Journal*, *10*(1), 180–204. https://doi.org/10.1007/s10040-001-0169-1

Gentine, P., Green, J. K., Guérin, M., Humphrey, V., Seneviratne, S. I., Zhang, Y., & Zhou, S. (2019). Coupling between the terrestrial carbon and water cycles—A review. *Environmental Research Letters*, *14*(8), 083003. https://doi.org/10.1088/1748-9326/ab22d6

George, N., Thompson, S. E., Hollingsworth, J., Orloff, S., & Kaffka, S. (2018). Measurement and simulation of water-use by canola and camelina under cool-season conditions in California. *Agricultural Water Management*, *196*, 15–23. https://doi.org/10.1016/j.agwat.2017.09.015

Gorelick, N., Hancher, M., Dixon, M., Ilyushchenko, S., Thau, D., & Moore, R. (2017). Google Earth engine: Planetary-scale geospatial analysis for everyone. *Remote Sensing of Environment*, *202*, 18–27. https://doi.org/10.1016/j.rse.2017.06.031

Guderle, M., & Hildebrandt, A. (2015). Using measured soil water contents to estimate evapotranspiration and root water uptake profiles–A comparative study. *Hydrology and Earth System Sciences*, *19*(1), 409–425. https://doi.org/10.5194/hess-19-409-2015

Gupta, H. V., Kling, H., Yilmaz, K. K., & Martinez, G. F. (2009). Decomposition of the mean squared error and nse performance criteria: Implications for improving hydrological modelling. *Journal of Hydrology*, *377*(1–2), 80–91. https://doi.org/10.1016/j.jhydrol.2009.08.003

Guswa, A. J. (2008). The influence of climate on root depth: A carbon cost-benefit analysis. *Water Resources Research*, *44*(2). https://doi.org/10.1029/2007wr006384

Hahm, W. J., Dralle, D., Rempe, D., Bryk, A., Thompson, S., Dawson, T., & Dietrich, W. (2019). Low subsurface water storage capacity relative to annual rainfall decouples mediterranean plant productivity and water use from rainfall variability. *Geophysical Research Letters*, *46*(12), 6544–6553. https://doi.org/10.1029/2019gl083294

Hahm, W. J., Dralle, D. N., Sanders, M., Bryk, A. B., Fauria, K. E., Huang, M.-H., et al. (2022). Bedrock vadose zone storage dynamics under extreme drought: Consequences for plant water availability, recharge, and runoff. *Water Resources Research*, *58*(4), e2021WR031781. https://doi.org/10.1029/2021wr031781

Hahm, W. J., Rempe, D., Dralle, D., Dawson, T., & Dietrich, W. (2020). Oak transpiration drawn from the weathered bedrock vadose zone in the summer dry season. *Water Resources Research*, *56*(11), e2020WR027419. https://doi.org/10.1029/2020wr027419

Hahm, W. J., Rempe, D. M., Dralle, D. N., Dawson, T. E., Lovill, S. M., Bryk, A. B., et al. (2019). Lithologically controlled subsurface critical zone thickness and water storage capacity determine regional plant community composition. *Water Resources Research*, *55*(4), 3028–3055. https://doi.org/10.1029/2018wr023760

Hargreaves, G. H., & Samani, Z. A. (1985). Reference crop evapotranspiration from temperature. *Applied Engineering in Agriculture*, *1*(2), 96–99. https://doi.org/10.13031/2013.26773

Hillel, D. (2003). *Introduction to environmental soil physics*. Elsevier.

Hupet, F., Lambot, S., Feddes, R., Van Dam, J., & Vanclooster, M. (2003). Estimation of root water uptake parameters by inverse modeling with soil water content data. *Water Resources Research*, *39*(11). https://doi.org/10.1029/2003wr002046

Jasechko, S., Birks, S. J., Gleeson, T., Wada, Y., Fawcett, P. J., Sharp, Z. D., et al. (2014). The pronounced seasonality of global groundwater recharge. *Water Resources Research*, *50*(11), 8845–8867. https://doi.org/10.1002/2014wr015809

Jasechko, S., Sharp, Z. D., Gibson, J. J., Birks, S. J., Yi, Y., & Fawcett, P. J. (2013). Terrestrial water fluxes dominated by transpiration. *Nature*, *496*(7445), 347–350. https://doi.org/10.1038/nature11983

Jobbagy, E. G., & Jackson, R. B. (2001). The distribution of soil nutrients with depth: Global patterns and the imprint of plants. *Biogeochemistry*, *53*(1), 51–77. https://doi.org/10.1023/a:1010760720215

Kleidon, A., & Heimann, M. (1998). A method of determining rooting depth from a terrestrial biosphere model and its impacts on the global water and carbon cycle. *Global Change Biology*, *4*(3), 275–286. https://doi.org/10.1046/j.1365-2486.1998.00152.x

Köppen, W., & Geiger, R. (1928). Climate classification world map.

Kosugi, Y., & Katsuyama, M. (2007). Evapotranspiration over a Japanese cypress forest. Ii. Comparison of the eddy covariance and water budget methods. *Journal of Hydrology*, *334*(3–4), 305–311. https://doi.org/10.1016/j.jhydrol.2006.05.025

Kumar, R., Shankar, V., & Jat, M. K. (2015). Evaluation of root water uptake models–A review. *ISH Journal of Hydraulic Engineering*, *21*(2), 115–124. https://doi.org/10.1080/09715010.2014.981955

La Follette, P. T., Hahm, W. J., Rempe, D. M., Dietrich, W. E., Brauer, C. C., Weerts, A. H., & Dralle, D. N. (2022). Multicriteria analysis on rock moisture and streamflow in a rainfall-runoff model improves accuracy of model results. *Hydrological Processes*, *36*(3), e14536. https://doi.org/10.1002/hyp.14536

Lai, Y., Tian, J., Kang, W., Guo, S., Zhou, Y., & He, C. (2023). Estimating evapotranspiration from soil moisture using the improved soil water balance method in cold mountainous areas. *Journal of Hydrology X*, *20*, 100154. https://doi.org/10.1016/j.hydroa.2023.100154

Lapides, D. A., Dralle, D. N., Hahm, W. J., Dietrich, W. E., & Rempe, D. M. (2024). Supporting data and code for root water uptake resolved by distributed storage changes through soil and weathered bedrock. Retrieved from https://github.com/lapidesd/ET_layers,doi=10.5281/zenodo.12537870

Lapides, D. A., Hahm, W. J., Forrest, M., Rempe, D. M., Hickler, T., & Dralle, D. N. (2023). Inclusion of bedrock vadose zone in dynamic global vegetation models is key for simulating vegetation structure and functioning. *EGUsphere*, 1–34.

Li, Y., Fuchs, M., Cohen, S., Cohen, Y., & Wallach, R. (2002). Water uptake profile response of corn to soil moisture depletion. *Plant, Cell and Environment*, *25*(4), 491–500. https://doi.org/10.1046/j.1365-3040.2002.00825.x

Link, P., Simonin, K., Maness, H., Oshun, J., Dawson, T., & Fung, I. (2014). Species differences in the seasonality of evergreen tree transpiration in a mediterranean climate: Analysis of multiyear, half-hourly sap flow observations. *Water Resources Research*, *50*(3), 1869–1894. https://doi.org/10.1002/2013wr014023

Liu, W., Li, P., Duan, W., & Liu, W. (2014). Dry-season water utilization by trees growing on thin karst soils in a seasonal tropical rainforest of xishuangbanna, southwest China. *Ecohydrology*, *7*(3), 927–935. https://doi.org/10.1002/eco.1419

Lobet, G., Couvreur, V., Meunier, F., Javaux, M., & Draye, X. (2014). Plant water uptake in drying soils. *Plant physiology*, *164*(4), 1619–1627. https://doi.org/10.1104/pp.113.233486

Maysonnave, J., Delpierre, N., François, C., Jourdan, M., Cornut, I., Bazot, S., et al. (2022). Contribution of deep soil layers to the transpiration of a temperate deciduous forest: Implications for the modelling of productivity. *Science of The Total Environment*, *838*, 155981. https://doi.org/10.1016/j.scitotenv.2022.155981

McCole, A. A., & Stern, L. A. (2007). Seasonal water use patterns of Juniperus ashei on the edwards Plateau, Texas, based on stable isotopes in water. *Journal of Hydrology*, *342*(3–4), 238–248. https://doi.org/10.1016/j.jhydrol.2007.05.024

McCormick, E. L., Dralle, D. N., Hahm, W. J., Tune, A. K., Schmidt, L. M., Chadwick, K. D., & Rempe, D. M. (2021). Widespread woody plant use of water stored in bedrock. *Nature*, *597*(7875), 225–229. https://doi.org/10.1038/s41586-021-03761-3

Musters, P., & Bouten, W. (1999). Assessing rooting depths of an Austrian pine stand by inverse modeling soil water content maps. *Water Resources Research*, *35*(10), 3041–3048. https://doi.org/10.1029/1999wr900173

Musters, P., & Bouten, W. (2000). A method for identifying optimum strategies of measuring soil water contents for calibrating a root water uptake model. *Journal of Hydrology*, *227*(1–4), 273–286. https://doi.org/10.1016/s0022-1694(99)00187-0

Nimmo, J. R. (2006). Unsaturated zone flow processes. *Encyclopedia of hydrological sciences*.

Oshun, J., Dietrich, W. E., Dawson, T. E., & Fung, I. (2016). Dynamic, structured heterogeneity of water isotopes inside hillslopes. *Water Resources Research*, *52*(1), 164–189. https://doi.org/10.1002/2015wr017485

Portmann, F. T., Döll, P., Eisner, S., & Flörke, M. (2013). Impact of climate change on renewable groundwater resources: Assessing the benefits of avoided greenhouse gas emissions using selected cmip5 climate projections. *Environmental Research Letters*, *8*(2), 024023. https://doi.org/10.1088/1748-9326/8/2/024023

Protopapas, A. L., & Bras, R. L. (1987). A model for water uptake and development of root systems. *Soil Science*, *144*(5), 352–366. https://doi.org/10.1097/00010694-198711000-00006

Querejeta, J. I., Estrada-Medina, H., Allen, M. F., Jiménez-Osornio, J. J., & Ruenes, R. (2006). Utilization of bedrock water by Brosimum alicastrum trees growing on shallow soil atop limestone in a dry tropical climate. *Plant and Soil*, *287*(1–2), 187–197. https://doi.org/10.1007/s11104-006-9065-8

Rempe, D. M., & Dietrich, W. E. (2014). A bottom-up control on fresh-bedrock topography under landscapes. *Proceedings of the National Academy of Sciences*, *111*(18), 6576–6581. https://doi.org/10.1073/pnas.1404763111

Rempe, D. M., & Dietrich, W. E. (2018). Direct observations of rock moisture, a hidden component of the hydrologic cycle. *Proceedings of the National Academy of Sciences*, *115*(11), 2664–2669. https://doi.org/10.1073/pnas.1800141115

Rose, K., Graham, R., & Parker, D. (2003). Water source utilization by Pinus jeffreyi and Arctostaphylos patula on thin soils over bedrock. *Oecologia*, *134*(1), 46–54. https://doi.org/10.1007/s00442-002-1084-4

Rothfuss, Y., & Javaux, M. (2017). Reviews and syntheses: Isotopic approaches to quantify root water uptake: A review and comparison of methods. *Biogeosciences*, *14*(8), 2199–2224. https://doi.org/10.5194/bg-14-2199-2017

Ruiz, L., Varma, M. R., Kumar, M. M., Sekhar, M., Maréchal, J.-C., Descloitres, M., et al. (2010). Water balance modelling in a tropical watershed under deciduous forest (Mule hole, India): Regolith matric storage buffers the groundwater recharge process. *Journal of Hydrology*, *380*(3–4), 460–472. https://doi.org/10.1016/j.jhydrol.2009.11.020

Salve, R., Rempe, D. M., & Dietrich, W. E. (2012). Rain, rock moisture dynamics, and the rapid response of perched groundwater in weathered, fractured argillite underlying a steep hillslope. *Water Resources Research*, *48*(11). https://doi.org/10.1029/2012wr012583

Schelde, K., Ringgaard, R., Herbst, M., Thomsen, A., Friborg, T., & Søgaard, H. (2011). Comparing evapotranspiration rates estimated from atmospheric flux and tdr soil moisture measurements. *Vadose Zone Journal*, *10*(1), 78–83. https://doi.org/10.2136/vzj2010.0060

Schenk, H. J., & Jackson, R. B. (2002). The global biogeography of roots. *Ecological Monographs*, *72*(3), 311–328. https://doi.org/10.2307/3100092

Schmidt, L., & Rempe, D. (2020). Quantifying dynamic water storage in unsaturated bedrock with borehole nuclear magnetic resonance. *Geophysical Research Letters*, *47*(22), e2020GL089600. https://doi.org/10.1029/2020gl089600

Schwinning, S. (2010). The ecohydrology of roots in rocks. *Ecohydrology: Ecosystems, land and water process interactions, Ecohydrogeomorphology*, *3*(2), 238–245. https://doi.org/10.1002/eco.134

Schymanski, S. J. (2007). *Transpiration as the leak in the carbon factory: A model of self-optimising vegetation (unpublished doctoral dissertation)*. University of Western Australia.

Schymanski, S. J., Sivapalan, M., Roderick, M. L., Beringer, J., & Hutley, L. B. (2008). An optimality-based model of the coupled soil moisture and root dynamics. *Hydrology and Earth System Sciences*, *12*(3), 913–932. https://doi.org/10.5194/hess-12-913-2008

Scott, R. L., Cable, W. L., & Hultine, K. R. (2008). The ecohydrologic significance of hydraulic redistribution in a semiarid savanna. *Water Resources Research*, *44*(2). https://doi.org/10.1029/2007wr006149

Simunek, J., Sejna, M., Van Genuchten, M. T., Simunek, J., Šejna, M., Jacques, D., & Sakai, M. (1998). Hydrus-1d. Simulating the one-dimensional movement of water, heat, and multiple solutes in variably-saturated media, version, 2.

Smith, B., Prentice, I. C., & Sykes, M. T. (2001). Representation of vegetation dynamics in the modelling of terrestrial ecosystems: Comparing two contrasting approaches within European climate space. *Global Ecology and Biogeography*, *10*(6), 621–637. https://doi.org/10.1046/j.1466-822x.2001.t01-1-00256.x

Song, L., Zhu, J., Li, M., & Yu, Z. (2014). Water utilization of Pinus sylvestris var. mongolica in a sparse wood grassland in the semiarid sandy region of northeast China. *Trees*, *28*(4), 971–982. https://doi.org/10.1007/s00468-014-1010-5

Sprenger, M., Leistert, H., Gimbel, K., & Weiler, M. (2016). Illuminating hydrological processes at the soil-vegetation-atmosphere interface with water stable isotopes. *Reviews of Geophysics*, *54*(3), 674–704. https://doi.org/10.1002/2015rg000515

U.S. Geological Survey. (2021). National water information system data available on the world wide web (water data for the nation)

Vrugt, J. A., Stauffer, P. H., Wohling, T., Robinson, B. A., & Vesselinov, V. V. (2008). Inverse modeling of subsurface flow and transport properties: A review with new developments. *Vadose Zone Journal*, *7*(2), 843–864. https://doi.org/10.2136/vzj2007.0078

Wada, Y., Wisser, D., & Bierkens, M. F. (2014). Global modeling of withdrawal, allocation and consumptive use of surface water and groundwater resources. *Earth System Dynamics*, *5*(1), 15–40. https://doi.org/10.5194/esd-5-15-2014

Wilson, K. B., Hanson, P. J., Mulholland, P. J., Baldocchi, D. D., & Wullschleger, S. D. (2001). A comparison of methods for determining forest evapotranspiration and its components: Sap-flow, soil water budget, eddy covariance and catchment water balance. *Agricultural and Forest Meteorology*, *106*(2), 153–168. https://doi.org/10.1016/s0168-1923(00)00199-4

Yang, D., Goodison, B. E., Metcalfe, J. R., Golubev, V. S., Bates, R., Pangburn, T., & Hanson, C. L. (1998). Accuracy of nws 8" standard nonrecording precipitation gauge: Results and application of wmo intercomparison. *Journal of Atmospheric and Oceanic Technology*, *15*(1), 54–68. https://doi.org/10.1175/1520-0426(1998)015<0054:aonsnp>2.0.co;2

Yang, G., Huang, L., & Shi, Y. (2022). Magnitude and determinants of plant root hydraulic redistribution: A global synthesis analysis. *Frontiers in Plant Science*, *13*, 918585. https://doi.org/10.3389/fpls.2022.918585

Zhang, F., & Zhang, C. (2021). Probing water partitioning in unsaturated weathered rock using nuclear magnetic resonance. *Geophysics*, *86*(5), WB131–WB147. https://doi.org/10.1190/geo2020-0591.1

Zhang, Y., Kong, D., Gan, R., Chiew, F. H., McVicar, T. R., Zhang, Q., & Yang, Y. (2019). Coupled estimation of 500 m and 8-day resolution global evapotranspiration and gross primary production in 2002–2017. *Remote Sensing of Environment*, *222*, 165–182. https://doi.org/10.1016/j.rse.2018.12.031

Zhang, Y., Peña-Arancibia, J. L., McVicar, T. R., Chiew, F. H., Vaze, J., Liu, C., et al. (2016). Multi-decadal trends in global terrestrial evapotranspiration and its components. *Scientific Reports*, *6*(1), 1–12.

References From the Supporting Information

Feng, X., Thompson, S. E., Woods, R., & Porporato, A. (2019). Quantifying asynchronicity of precipitation and potential evapotranspiration in mediterranean climates. *Geophysical Research Letters*, *46*(24), 14692–14701. https://doi.org/10.1029/2019gl085653

Gan, R., Zhang, Y., Shi, H., Yang, Y., Eamus, D., Cheng, L., et al. (2018). Use of satellite leaf area index estimating evapotranspiration and gross assimilation for Australian ecosystems. *Ecohydrology*, *11*(5), e1974. https://doi.org/10.1002/eco.1974

Tune, A. K., Druhan, J. L., Wang, J., Bennett, P. C., & Rempe, D. M. (2020). Carbon dioxide production in bedrock beneath soils substantially contributes to forest carbon cycling. *Journal of Geophysical Research: Biogeosciences*, *125*(12), e2020JG005795. https://doi.org/10.1029/2020jg005795